ARTICLE

An FGFR-p53 developmental signaling axis drives salivary cancer progression

Adele M. Musicant[1,15], Julia M. R. Billington[2,3,15], Jeffrey S. Damrauer[4], Jennifer L. Modliszewski[5], Luane J. B. Landau[6], Yi-Hsuan Tsai[5], Jay H. Mehta[3], John Powers[3], Renee Betancourt[7], Radhika Sekhri[8], Ricardo J. Padilla[9], Juan C. Hernandez-Prera[10], D. Neil Hayes[8], Trevor G. Hackman[11], Omer Gokcumen[6], Sarah M. Knox[12,13] and Antonio L. Amelio[3,14]✉

Mucoepidermoid carcinoma (MEC) is the most frequently occurring salivary gland malignancy. Here, we investigated transcriptomic profiles of human fetal and adult salivary glands and MEC tumors to assess programs involved in MEC progression. Molecular and genetic analyses revealed that MEC tumors and fetal salivary glands share proliferative and developmental gene expression profiles that implicate an FGFR-p53 signaling axis in salivary MEC progression. Based on these findings, we developed a genetically engineered mouse model of advanced MEC via targeted expression of the CRTC1-MAML2 oncogene in salivary ductal cells. Specifically, CRTC1-MAML2 expression combined with p53 dysregulation in salivary ducts rewires FGF signaling to drive formation of tumors with histological and molecular features of high-grade MEC. The combined bioinformatics and mouse modeling of this study demonstrate that salivary MEC progression is underpinned by reactivation of developmental signaling programs and suggests a role for FGFR targeted therapies in the treatment of high-grade MEC.

Oncogene (2025) 44:2876–2892; https://doi.org/10.1038/s41388-025-03444-7

Graphical Abstract

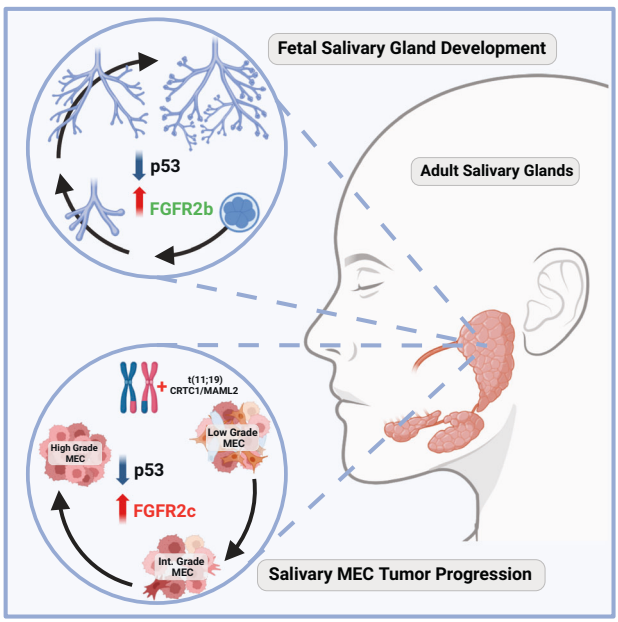

INTRODUCTION

Development and regulation of cellular heterogeneity within tumors has been attributed to several factors including the genetic and epigenetic landscape, tissue microenvironment context, and the tumor initiating cell of origin [1–9]. Moreover, master transcription factors with roles in lineage specification during normal development have been implicated in the regulation of tumor cell plasticity and the appearance of

A full list of author affiliations appears at the end of the paper.

Received: 19 November 2024 Revised: 1 May 2025 Accepted: 12 May 2025
Published online: 2 June 2025

heterogeneous tumor phenotypes [1–3, 8, 9]. Among these transcription factors, cAMP-Response Element Binding protein (CREB) plays a crucial role during development and its aberrant activity has been implicated in tumorigenesis [10–17]. Notably, salivary gland tumors are among the most diverse and heterogeneous neoplasms with mucoepidermoid carcinomas (MECs) representing the most common type of malignant salivary tumor. MECs also display an astonishing diversity in cellular phenotypes due to a pathognomonic transcriptional coactivator fusion (CRTC1-MAML2) that targets CREB and has been linked to this cellular heterogeneity [18].

Over 50% of salivary MEC tumors are characterized by the t(11;19) chromosomal translocation [19], which fuses the cyclic AMP (cAMP)-regulated transcriptional coactivator 1 (*CRTC1*) gene to the mastermind-like 2 (*MAML2*) gene. This translocation generates the oncogenic fusion CRTC1-MAML2 (C1/M2) which cell and murine models have revealed to be the etiologic factor driving emergence of salivary MEC [20–23]. As a potent coactivator of the master transcription factors CREB [21] and myelocytomatosis proto-oncogene (MYC) [24], C1/M2 regulates multiple signaling cascades important for tumor growth and progression including aberrant expression of insulin-like growth factor 1 (IGF-1), which has known roles in normal tissue development and growth but also tumorigenesis [25]. C1/M2-mediated dysregulation of transcriptional programs involved in normal development has been proposed to occur within a multipotent progenitor cell, likely a stem or reserve cell type within the salivary gland, which then differentiates into the other cell types present within MEC tumors [18, 26].

Histologically, salivary MEC tumors are characterized by up to eleven distinct cell types, although the presence of three main cell types (epidermoid, mucous, and intermediate cells) is typical and important in both diagnosis and prognosis [18]. MEC tumors are classified into three grades (low, intermediate, or high), depending on the presence of various pathological features, including the proportion of each of these three main cell types, perineural invasion, necrosis, and the number of mitotic cells [27–29]. Specifically, low-grade tumors tend to present with greater numbers of mucous cells and distinct cystic structures, and patients with these tumors generally have a >90% five-year survival rate. In contrast, high-grade tumors are typically characterized by increased mitotic activity as well as greater numbers of intermediate and epidermoid cell types [18, 30–32]. While low-grade tumors can be successfully managed with surgical resection, patients with high-grade tumors have five-year survival rates that plummet to <30% due to limited treatment options. Thus, understanding the mechanisms that control cellular heterogeneity and progression to high-grade disease in salivary MEC is crucial for identifying novel therapeutic vulnerabilities.

Tumor progression has been linked to regulation of transcriptional programs typically involved in normal development. To investigate the transcriptional framework regulating salivary MEC progression, we performed a comprehensive analysis of gene expression data from normal human fetal and adult salivary gland tissues compared to salivary MEC tumors of various grades. We show that high-grade tumors and developing fetal salivary glands are characterized by the regulation of the p53 pathway and demonstrate using a novel autochthonous genetically engineered mouse model that this impacts tumor plasticity and progression to high-grade disease. Furthermore, computational and molecular analyses of both human and murine salivary MEC tumors reveal that differential alternative splicing of FGFR2 distinguishes C1/M2-positive MEC tumors from transcriptional programs operational in normal fetal development. These findings identify potential therapeutic vulnerabilities of advanced salivary MEC to selective inhibitors of FGFR2.

MATERIALS AND METHODS

Clinical samples

All research involving human tumor tissues was reviewed and approved by The University of North Carolina at Chapel Hill Institutional Review Board under IRB protocols 15-1604 and 17-2947 and all participants provided informed consent for scientific research. Parotid gland tissues were randomly selected from de-identified clinical subjects identified by chart review. Archived formalin-fixed paraffin-embedded (FFPE) parotid salivary MEC ($n = 23$; 14 females, 9 males, average age of 52.2 years; 1 sex and age unavailable) or normal parotid salivary gland ($n = 8$) tissue samples were stored at room temperature for less than ten years before blocks were sectioned and RNA isolation was performed. For all cases, multiple hematoxylin and eosin (H&E) slides were reviewed by a pathologist and sections containing tumor were selected for inclusion in the study. Adjacent serial unstained sections were then macrodissected and tumor material submitted for RNA extraction. All research fetal salivary parotid gland tissues ($n = 3$) were reviewed and approved were by the University of California San Francisco (UCSF), as outlined in Saitou [33] et al. [33] Samples were collected post-mortem from fetuses between 22 and 24 weeks of gestation under IRB protocol 10-00768 [33].

Clinical RNA isolation

FFPE tissue samples were sent to the UNC Lineberger Comprehensive Cancer Center Translational Genomics Lab (TGL) for RNA isolation using the Maxwell 16 MDx Instrument (Promega AS3000) and the Maxwell 16 LEV RNA FFPE Kit (Promega AS1260) according to the manufacturer's protocol (Promega 9FB167). Pathology review of an H&E-stained slide was used to guide macro-dissection of unstained slides to enrich for tumor RNA. Total RNA quality was measured using a NanoDrop spectrophotometer (Thermo Scientific ND-2000C) and a TapeStation 4200 (Agilent G2991AA). Total RNA concentration was quantified using a Qubit 3.0 fluorometer (Life Technologies Q33216).

RNAseq

For human salivary MEC samples, total RNA sequencing libraries were prepared at TGL using a Bravo Automated Liquid-Handling Platform (Agilent G5562A) and the TruSeq Stranded Total RNA Library Prep Gold Kit (Illumina 20020599) according to the manufacturer's protocol (Illumina 1000000040499). RNAseq library quality and quantity were measured using a TapeStation 4200 (Agilent G2991AA), pooled at equimolar ratios and denatured according to the manufacturer's protocol (Illumina 15050107). Sequencing was performed at the High Throughput Sequencing Facility (HTSF) at UNC Chapel Hill. Two RNAseq libraries were sequenced per lane on a HiSeq2500 (Illumina SY–401–2501) with 2 × 50 bp paired-end configuration according to the manufacturer's protocol (Illumina 15035786). Sequencing performed at UCSF on RNA isolated from human adult and fetal tissue samples was performed according to GENEWIZ procedures using an Illumina HiSeq with a 2 x 150bp configuration according to methods outlined in Saitou et al. [33] For mouse salivary MEC samples, RNA was prepped from fresh, frozen tissues (control = 4; GEMM MEC = 4). Samples were prepared with Illumina TruSeq total RNA with Ribo-Zero Gold. Sequencing was performed with HiSeq 4000 with 2×150 bp paired-end read configuration.

RNAseq data processing

Raw FASTQ files for the UCSF [33] samples were downloaded from the sequence read archive database (SRA PRJNA601418) and the UCSF and UNC FASTQ files were processed together. Paired-end reads were trimmed of adaptors and low-quality bases via fastp v0.23.2 [34]. Default parameters for trimming were utilized with fastp automatic adaptor detection invoked. Trimmed fastq files were aligned to the GRCh38.d1.vd1 version of the human genome with GENCODE v36 version of the human transcriptome using STAR 2.7.6a [35]. Quantification of expression for each sample was performed using Salmon v1.4.0 [36]. Genes were retained for subsequent analysis if they contained more than 10 reads of raw counts in at least three samples. Normalization was performed using the DESeq2 v1.38.0 Bioconductor package in R v4.2.2 [37, 38]. To account for potential institution-specific variation, batch correction was performed via linear regression on log2 + 1 normalized counts (residuals following regression of platform on gene, followed by addition of per gene mean).

Bioinformatic analyses

Differential expression analysis was performed on linear regression-adjusted counts by fitting a linear model for each analysis, followed by

empirical Bayes moderation of the test statistics in the limma package. Principal component analyses were performed on log2-normalized unadjusted counts and batch-adjusted counts. The false discovery rate was calculated to control for multiple hypothesis testing. Gene set enrichment analysis was performed using the fgsea (v1.24.0) Bioconductor package to identify gene ontology terms and pathways associated with altered gene expression for each of the comparisons performed [39]. Hallmark pathways and C2 and C5 gene sets were downloaded from MSigDB (v2023.1) [39, 40]. Gene set enrichment analysis was performed using the clusterProfiler (v4.10.1) The proliferation-related gene sets, *GOBP Regulation of Cell Population Proliferation* and *GOBP Epithelial Cell Proliferation Involved in Salivary Gland Morphogenesis*, from the Molecular Signatures Database (MSigDB) were excluded from the ranked gene lists for Fetal versus Adult Tissue and MEC Tumors versus Adult Tissue comparisons. Gene Set Enrichment Analysis (GSEA) was then performed on these refined gene lists across all Hallmark pathways in MSigDB using clusterProfiler (v4.10.1). Bioconductor package to identify pathways associated with FGFR expression. The C2 gene sets for FGF/FGFR expression were downloaded using the msigdbr (v7.5.1) package.

Alternative splicing analyses

rMATs. Raw FASTQ reads were aligned to the GRCh38.d1.vd1 version of the human genome [41] using STAR 2.5.3a without trimming. rMATs (v4.1.2) [42] was run separately for each comparison (tumor vs normal, fetal vs normal, and fetal vs tumor), with a bam file provided for each sample within the group. Read length was set to be the average across all samples used in the analysis and variable read lengths were allowed.

Untrimmed Bam files from rMATs analyses were converted to BigWig files for visualization purposes via deepTools (v3.5.3) [43].

Formula (1) describes the Percent Spliced In (PSI, ψ) measure of exon inclusion level where ψ is calculated from the number of reads mapped to the exon inclusion isoform (I), the number of reads mapped to the exon skipping isoform (S), the effective length of the exon inclusion isoform (LI), and the effective length of the exon skipping isoform (LS), as per methods described in Roulis et al. [44].

$$\psi = \frac{\left(\frac{I}{LI}\right)}{\left(\frac{I}{LI} + \frac{S}{LS}\right)} \quad (1)$$

Troester p53 signature analysis

The Troester et al. [45] *TP53* mutation signature was applied the median centered, normalized and linear regression batch-adjusted RNAseq data. The per sample Spearman correlation to the signature was calculated as previously described [46]. Box plots were generated, with boxes representing the interquartile range with the median shown by the midline. Wilcoxon-rank sum test was performed to test for differences between all pairwise comparisons.

Generation of CreER-regulated CRTC1-MAML2 transgenic mice, genotyping, and tamoxifen administration

All animal studies were approved by the Institutional Animal Care and Use Committee (IACUC) of The University of North Carolina Chapel Hill, Moffitt Cancer Center and the University of South Florida. The *Dcpp1-CreER* (MGI:5661581) and *Mist1-CreER* mouse strains were generously provided by Dr. Catherine Ovitt (University of Rochester) [47, 48]. *KRT14-CreER* (Stock #005107) mice were obtained from the Jackson Laboratory. Rosa26-LSL-GpNLuc (LumiFluor) mice were generated by knocking in GpNLuc LumiFluor optical reporter [49] cDNA into a Rosa26-LoxP-STOP-LoxP cassette, as described by Carper et al. [50] The CRTC1-MAML2 transgenic mouse line was generously provided by Dr. Lizi Wu (University of Florida) [20]. *Trp53* floxed mice were obtained from the National Cancer Institute Mouse Repository (Strain #01XC2). All mice were carried on an albino B6(Cg)-Tyr$^{c\text{-}2J}$/J (The Jackson Laboratory, Stock #000664 or Stock #000058) background after 7–10 rounds of backcrossing. *Dcpp1-CreER* and *Mist1-CreER* alleles were maintained at heterozygosity; all other alleles were bred to either heterozygosity or homozygosity. Tail snips (< 3 mm in size) were rinsed in isopropanol and sent to Transnetyx (Memphis, TN) for genotyping using qPCR. Probes used for genotyping were established from primer sets obtained from The Jackson Laboratory or Mouse Genome Informatics (MGI). For murine lines established in-house, primer sets were provided to Transnetyx to develop probes.

Tamoxifen (Sigma-Aldrich #T5648) was dissolved at 10 mg/mL in corn oil (MP Biomedical #901414). To conditionally induce CRTC1-MAML2 and LumiFluor expression and to flox out p53 alleles, 8-week-old male and female animals were intraperitoneally (i.p.) injected with 100 µL tamoxifen once a day for five consecutive days. Studies were not conducted blindly. Males and females at 8 weeks were randomly assigned for GEMM studies and similar findings are reported for both sexes. The number of mice used per group was based on prior related studies evaluating similar phenotypes and no statistical method was used to predetermine sample size.

Bioluminescence imaging

Bioluminescent-fluorescent BRET signal was measured non-invasively as previously described [49] with minor modification. Briefly, animals were i.p. injected with 250 µM (1:20 dilution, ~500 µg/kg) Nano-Glo Luciferase Assay Substrate (Promega, cat. #N1120) in sterile PBS. Isoflurane-anesthetized animals were then imaged using an AMI Optical Imaging System (Spectral Instruments Imaging, Inc.) 5 min after injection. Images were captured with an open filter and acquisition times of 5 min or less at the indicated settings. Data were analyzed using Aura imaging software (v2.2.0.0).

Histology and immunohistochemistry

All animals showing obvious tumors or other signs of distress were euthanized and subjected to full necropsy. For histological analysis, all tissues (including submandibular glands, sublingual glands, parotid glands, pancreas, and lungs) were fixed in 10% buffered formalin for approximately 1 week at room temperature. Following fixation, tissues were processed on an ASP6025 automated tissue processor (Leica Biosystems) and embedded in paraffin wax. Blocks were sectioned at 4–6 µm, mounted on glass slides, and FFPE tissue sections were deparaffinized prior to staining using Dewax Solution (Leica). H&E staining was performed using pre-mixed hematoxylin, clarifier, bluing reagent, and eosin (Richard Allan Scientific). Heat-induced antigen retrieval method was performed in Epitope Retrieval Solution 2 (Leica).

Ki-67 rabbit antibody (Abcam ab16667, Cambridge, MA) was used at a 1:2000 concentration in Dako antibody diluent (Carpinteria, CA) and incubated for 15 min. Cleaved Caspase-3 rabbit antibody (CST 9661, Danver, MA) was used at a 1:1000 concentration in Dako antibody diluent (Carpinteria, CA) and incubated for 15 min. pERK1/2 (T202/Y204) rabbit antibody (CST 4370, Danvers, MA) was used at a 1:2000 concentration in Ventana PSS antibody diluent (Tuscon, AZ) and incubated for 30 min. pAKT (S473) rabbit antibody (Abcam ab81283, Cambridge, MA) was used at a 1:200 concentration in Ventana PSS antibody diluent (Tucson, AZ) and incubated for 30 min. Slides were incubated for 8 min using the Leica Bond Polymer Refine Detection System and then counterstained with hematoxylin. Slides were then dehydrated and cover slipped as per normal laboratory protocol.

Ki-67, Cleaved Caspase-3, p-ERK1/2, and p-AKT IHC stained slides were scanned using the Aperio™ ScanScope AT2 (Leica Biosystems, Vista, CA) with a 20x/0.8NA objective lens. Images were accessed via Aperio's eSlide manager database and viewed with Imagescope version 12.4.3.5008 [51]. Each image was annotated in Imagescope with the manual drawing tools to create Regions of Interest (ROIs) for multiple tissue subtypes, which include lung, pancreas, parotid, submandibular gland, and sublingual gland. Each of these ROIs was analyzed using a prebuilt Aperio algorithm to quantify objects into four categories (negative, weak, moderate, and strong) based on the staining intensity. Finally, the data for each ROI was exported into Microsoft Excel where percent positivity and H-scores were calculated based on the object counts for each stain intensity category.

Polymerase chain reaction (PCR) and qPCR

For fresh-frozen tissues, gene expression was measured by extracting RNA using a Nucleospin RNA kit (Machery-Nagel #740955) according to the manufacturer's instructions. cDNA was synthesized from 1 µg of RNA using the iScript cDNA synthesis kit (Bio-Rad #170-8890). For human tissues, RNA was extracted using the Maxwell 16 LEV RNA FFPE Kit (Promega #AS1260) according to the manufacturer's protocol (Promega 9FB167). cDNA was made from 1 to 4 µg of RNA using SuperScript IV Reverse Transcriptase (Invitrogen #18090050) with dNTPs (NEB #N0446S), RNase inhibitor (Applied Biosystems #N808-0119), 25 µM oligo d(T)20 primer (Invitrogen #100023441), and 25 µM MAML2-specific reverse primer. C1/M2 copy number was determined by establishing standard curves with 100 to 1×10^6 copies of a FLAG-tagged C1/M2 overexpression plasmid [52].

Relative gene expression of *C1/M2* was determined using the $2^{(-\Delta\Delta Ct)}$ method and normalized to human *RPL23* expression. The same $2^{(-\Delta\Delta Ct)}$ method was used for the analysis of *Fgfr2*, *Fgfr2b*, and *Fgfr2c* and normalized to mouse *Rpl23*. qPCR was performed using FastStart Universal SYBR Green Master (Rox) Mix (Roche #04913850001) with 1/50 (tissue) or 1/100 (cells) volume of the cDNA iScript reaction, and 0.25 μM of primers. All PCR and qPCR primers are listed along with their sequences in Supplementary Table S3 [25, 53].

Quantification and statistical analyses

All statistical tests were conducted using GraphPad Prism software or the statistical software R (version 3.1.2). Differences between variables were assessed by 2-tailed Student's *t* test or 2-way ANOVA with Bonferroni's post hoc tests, where appropriate. No data were excluded from the analysis. Sample sizes and *P* values are shown in figure legends. Normal distribution of samples was not determined. Data collection and analyses were not performed blind to the conditions of the experiment. Data are presented as mean ± SD or mean ± SEM, as indicated in the figure legends. *P* values < 0.05 were considered statistically significant ($^{*}P < 0.05$, $^{**}P = 0.001$, $^{***}P < 0.001$).

Materials and availability

The mouse strains described in this study are available from the Corresponding Author upon request via a material transfer agreement (MTA).

RESULTS

Transcriptional programs driving development are operational in salivary MEC

Previous studies have demonstrated that cancer cells may exhibit gene expression signatures similar to those found in fetal cells and tissues [45, 54, 55]. Additionally, those shared expression signatures have been shown in some cases to be associated with disease progression and patient prognosis [56]. Prior work from our group identified gene expression signatures common to salivary gland development and salivary MEC [24, 25], however the relationship between these shared signatures and disease progression has yet to be determined. To this end, we performed RNA sequencing (RNAseq) on a cohort of 23 human salivary MEC tumors (Table 1), 8 normal adult salivary glands, and 3 normal fetal salivary glands (22–24 weeks of age) and identified differentially expressed genes (DEGs; fold change ≥2.00) for fetal or tumor tissues relative to adult tissues. Relative to normal adult salivary glands, MEC tumor samples exhibited 1989 downregulated and 1566 upregulated genes (Fig. 1A and Supplementary Table S1) and fetal salivary gland samples exhibited 2007 downregulated and 1331 upregulated genes (Fig. 1B).

Of these DEGs, 797 upregulated genes and 1312 downregulated genes were directionally similar in both the MEC tumor samples and fetal salivary samples as compared to normal adult salivary glands (Fig. 1C). iRegulon [57] analysis of gene regulatory networks predicted that the shared upregulated genes were enriched in binding sites for specific transcription factors such as E2F transcription factor 4 (E2F4), forkhead box M1 (FOXM1), and transcription factor Dp-1 (TFDP1), among others, indicating common gene regulation by these transcription factors (Fig. 1D). iRegulon analysis of the shared downregulated genes revealed an enrichment of predicted transcription factor binding sites for jun proto-oncogene (JUN), myogenin (MYOG), and lysine demethylase 5 (KDM5), among others (Fig. 1D). Gene set enrichment analysis (GSEA) identified hallmark gene signatures and biological processes that were significantly altered in MEC tumors and fetal salivary glands compared to adult salivary glands (Fig. 1E, F and Supplementary Fig. S1). Many of the identified pathways were shared between MEC tumors and fetal salivary glands, including upregulation of genes encoding proteins involved in the epithelial-mesenchymal transition, angiogenesis, and cell cycle and downregulation of genes encoding proteins that function in DNA repair and protein secretion (Fig. 1E, F). Notably, the p53 pathway was downregulated (normalized enrichment score [NES] <−1.50) in fetal tissue compared with adult salivary glands (Fig. 1F).

Regulation of the p53 pathway is a hallmark of fetal salivary glands and high-grade MEC

The C1/M2 fusion event has been previously shown to be a pathognomonic driver of low-grade MEC [19]; however, its role in the etiology of high-grade MEC has not been established. To determine whether high-grade MEC tumors express C1/M2, we first performed quantitative polymerase chain reaction (qPCR) for C1/M2 in our human tumor samples and found that all the low-grade and slightly less than half of the high-grade MEC samples in our cohort were C1/M2-positive (Fig. 2A). Fluorescence in situ hybridization (FISH) using a break-apart probe targeting the *MAML2* gene locus confirmed the presence of the t(11;19) translocation in low-grade and high-grade MEC samples (Fig. 2B and Table 1) as well as in established MEC cell lines (Supplementary Fig. S2A), supporting a role for C1/M2 expression across multiple stages of salivary MEC progression.

To investigate the relationship between gene expression patterns in fetal development and tumor progression, principal component analysis on bulk RNAseq data was performed and revealed that C1/M2-positive high-grade MEC tumor samples are more similar to developing fetal salivary glands than to normal adult salivary glands (Fig. 2C). Therefore, we analyzed DEGs specifically in high-grade and low-grade MEC samples or fetal salivary glands relative to normal adult salivary gland tissues. This analysis identified 364 upregulated (logFC ≥2.00) and 733 downregulated genes (logFC ≤−2.00) common to all three sample groups (Fig. 2D). However, a greater number of downregulated genes were uniquely shared between fetal samples and high-grade MEC (361 genes) than between fetal samples and low-grade MEC (116 genes) (Fig. 2D). Notably, application of iRegulon to detect genes which contain common transcription factor binding sites in their cis-regulatory control elements identified FOXM1 motif enrichment among the upregulated genes (Fig. 1D). FOXM1 is a pro-proliferative transcription factor negatively regulated by the tumor suppressor p53 (Supplementary Fig. S2B) [58, 59]. While the logFC level for *FOXM1* did not reach the threshold of logFC of ≥2.00, the logFC level was 1.932 in fetal samples (FC = 3.816), 1.862 in High Grade MEC samples (FC = 3.635), and 0.438 in Low Grade MEC (FC = 1.355), suggesting that p53 dysregulation is associated with tumor progression. Further analysis confirmed that *FOXM1* transcript levels are significantly increased in fetal salivary glands and high-grade MEC tumor samples ($P < 0.05$ and $P < 0.001$, respectively) when compared to adult samples regardless of C1/M2 fusion status (Fig. 2E).

Several studies have documented a role for tumor protein p53 (*TP53*) loss in the progression of pancreatic cancer [60], which displays histologic similarities with salivary MEC. While mutational profiling studies revealed that fusion negative salivary MEC tumors may harbor p53 genomic alterations associated with poor prognosis [61, 62], comparatively few genomic alterations are seen in C1/M2 fusion positive cases and p53 is frequently wildtype. However, p53 pathway dysregulation commonly occurs via transcriptional repression and/or overexpression of the mouse double minute 2 (*MDM2*) gene and previous studies have demonstrated that targeting MDM2 with the novel small molecule inhibitor MI-773 can stabilize and reactivate p53 signaling [63–65]. To assess functionality of the p53 pathway, we leveraged the p53 pathway dysregulation signature from Troester et al. [64] The Troester 52 gene signature was derived from the union of genes that displayed significant differential expression as a result of in vitro *TP53* knockdown in isogenic cell lines and genes that were differentially expressed between human p53 intact and p53 altered breast tumors. To evaluate the p53 status of a given sample, a Pearson correlation to the Troester signatures was calculated, with a positive correlation indicating p53 disfunction and negative correlation indicating wild type p53 functional

Table 1. Demographics of human salivary mucoepidermoid carcinoma cases.

Sample name	Patient age, yr	Patient sex	Tumor grade	Fusion status (qPCR)	FISH validation	Tumor location	Surgical treatment	Stage	Adjuvant therapy[a]	Recurrence	RNAseq performed
hT1	8	F	Low	Positive	No	Right parotid	Right superficial parotidectomy	NA	N/A	No	Yes
hT2	26	M	Low	Positive	No	Left parotid	Left superficial parotidectomy with facial nerve dissection	T3N1	XRT	No	Yes
hT3	34	F	Low	Positive	No	Left parotid	Left parotidectomy	pT2Nx	XRT	No	Yes
hT4	49	F	Low	Positive	No	Right parotid	Right superficial parotidectomy	pT2N2bM0	XRT	Yes	Yes
hT5	44	M	Low	ND	No	Right parotid	Parotidectomy	pT1N0	N/A	No	Yes
hT6	54	F	Low	Positive	Yes	Right parotid	Superficial parotidectomy	pT1N0	N/A	No	Yes
hT7	33	F	Low	Positive	No	Right parotid	Parotidectomy and right neck dissection	pT3N1	XRT	No	Yes
hT8	33	F	Low	Positive	Yes	Right parotid	Resection of tumor	NA	XRT	No	Yes
hT9	47	M	High	Negative	Yes	Left parotid	Total parotidectomy and neck dissection	NA	XRT	No	Yes
hT10	43	F	High	Negative	No	Right parotid	Superficial parotidectomy	T4N0Mx	XRT	No	Yes
hT11	77	F	High	Negative	Yes	Left parotid	Left superficial parotidectomy, partial resection	NA	XRT	No	Yes
hT12	66	M	High	Negative	No	Right parotid	Right parotidectomy	T3N0M0	XRT	No	Yes
hT13	85	M	High	Negative	Yes	Right parotid	Right parotidectomy		XRT	Yes	Yes
hT14	46	F	High	Negative	No	Left parotid	Left parotidectomy, left radical neck dissection, left hemimandibulectomy, left lateral temporal bone resection	T4aN2bM0	XRT + weekly carboplatin	No	Yes
hT15	61	M	High	Positive	No	Left parotid	Left partial parotidectomy followed by left neck dissection	pT2NxMx	XRT + weekly cisplatin	Unknown	Yes
hT16	57	F	High	Negative	No	NA	NA	NA	XRT + weekly cisplatin	Yes	Yes
hT17	64	M	High	Positive	No	Right parotid	Total right parotidectomy, lateral temporal bone resection	pT4aN2bMx	XRT	Yes	Yes
hT18	66	M	High	Positive	No	Right parotid	Tumor resection	pT1N0	NA	No	Yes
hT19			High	Positive	Yes	Not specified	NA	NA	NA	NA	Yes

Table 1. continued

Sample name	Patient age, yr	Patient sex	Tumor grade	Fusion status (qPCR)	FISH validation	Tumor location	Surgical treatment	Stage	Adjuvant therapy[a]	Recurrence	RNAseq performed
hT20	56	F	High	Negative	Yes	Left parotid	Left radical parotidectomy with extradural and temporal resection of tumor with cable nerve harvest and graft of the 7th facial nerve with a left modified radical neck dissection.	NA	NA	NA	Yes
hT21	27	F	High	Positive	No	Base of tongue	Excision of mass at base of tongue	T2N0M0	Postoperative RT and concurrent chemotherapy	Yes	Yes
hT22	58	F	High	Positive	Yes	Left SMG	Radical left neck dissection and right level 1 (which includes SMG)	pT3N3b	NA	NA	Yes
hT23	82	F	Low	ND	Yes	Right posterior mandible	En bloc resection of right retromolar trigone region of the mandible	ND	NA	No	No
hT24	85	M	Low	ND	Yes	Right parotid	Right parotidectomy with facial nerve dissection and facial nerve monitoring with excision of deep lobe parotid tumor	ND	NA	No	No

[a]Patients in this cohort did not receive neoadjuvant therapy.

FISH fluorescence in situ hybridization, *hT* human tumor, *MEC* mucoepidermoid carcinoma, *ND* not determined, *NA* not available, *qPCR* quantitative polymerase chain reaction, *RNAseq* RNA sequencing, *SMG* submandibular gland, *XRT* radiation therapy.

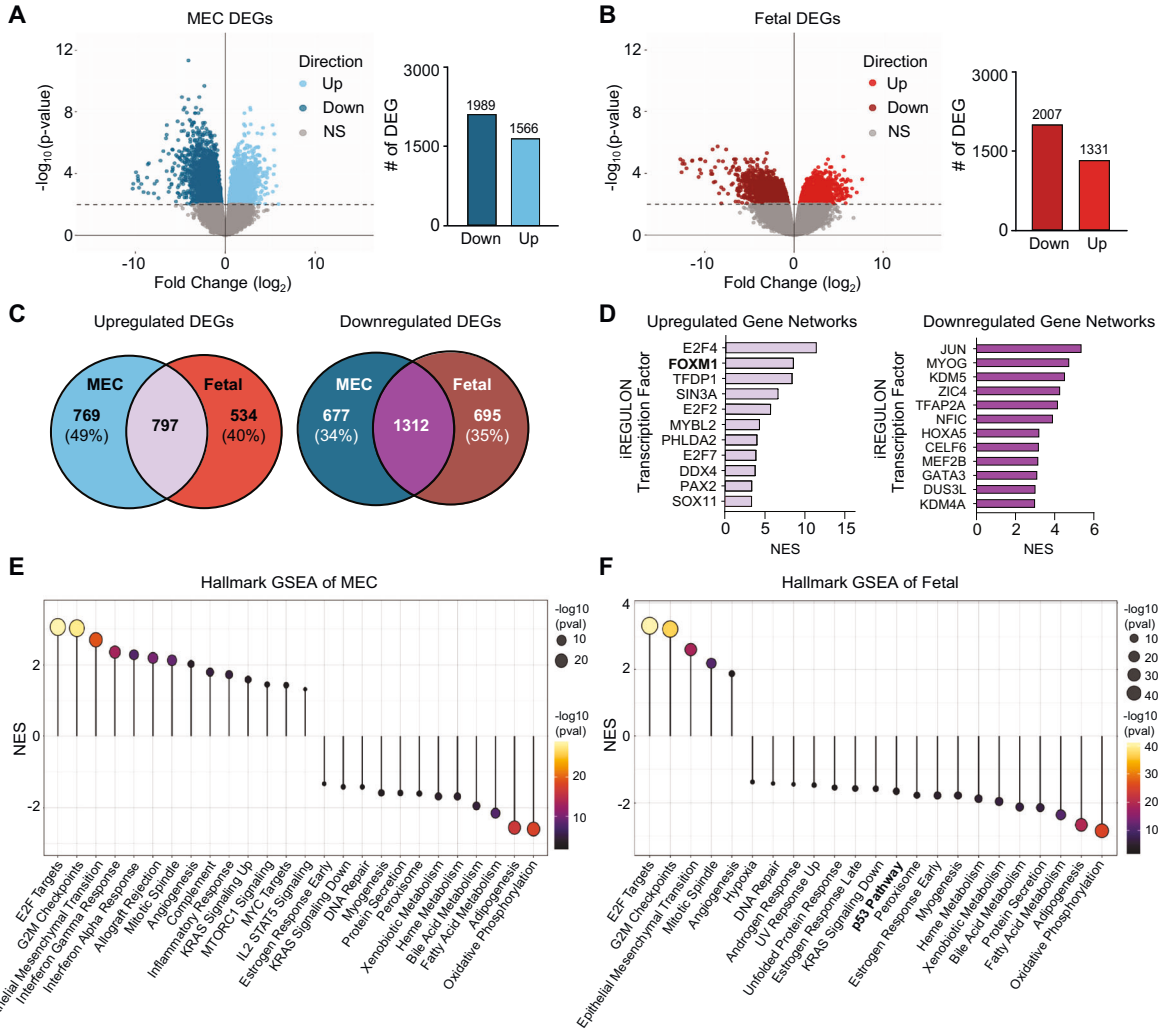

Fig. 1 Fetal salivary glands and salivary MEC tumors share related transcriptional programs. A DEG analysis of MEC tumor tissue vs normal adult parotid tissue. (*Left*) Volcano plot showing the relative expression of genes in each sample type. The dotted line represents $P_{adj} = 0.010$. Colored points above the line indicate DEGs with $P_{adj} < 0.010$. (*Right*) Quantification of the colored points from the volcano plot. The bar chart shows the number of upregulated (FC ≥ 2.00) and downregulated (FC ≤ −2.00) genes with $P_{adj} < 0.010$. **B** DEG analysis of fetal parotid tissue vs normal adult parotid tissue. (*Left*) Volcano plots showing the relative expression of genes in each sample type. The dotted line represents $P_{adj} = 0.010$. Colored points above the line indicate DEGs with $P_{adj} < 0.010$. (*Right*) Quantification of the colored points from the volcano plot. The bar chart shows the number of upregulated (FC ≥ 2.00) and downregulated (FC ≤ −2.00) genes with $P_{adj} < 0.010$. **C** Venn diagrams showing the number of DEGs identified in MEC tumors only (blue), fetal salivary glands only (red), and both (purple). Percentages reflect non-overlapping DEGs. **D** iRegulon-predicted transcription factor regulators of upregulated (*left*) and downregulated (*right*) DEG networks common to both MEC tumors and fetal salivary glands. **E** Hallmark GSEA pathway enrichment analysis showing upregulated and downregulated DEG pathways in MEC tumors vs adult parotid tissue. Only pathways with NES ≥ 1.50 or ≤−1.50 are displayed. Node size is proportional to the -$\log_{10}$(padj) values. **F** Hallmark GSEA pathway enrichment analysis showing upregulated and downregulated DEG pathways in fetal vs adult parotid tissue. Only pathways with NES ≥ 1.50 or ≤−1.50 are displayed. Node size is proportional to the -$\log_{10}$(padj) values. DEG differentially expressed gene, FC fold change, GSEA gene set enrichment analysis, MEC mucoepidermoid carcinoma, NES normalized enrichment score, NS not significant, SG salivary gland.

status. We examined these 'p53-dysregulation' and 'p53-wildtype' signatures in our fetal and adult salivary MEC samples relative to normal adult salivary glands and observed a statistically significant upregulation of the dysregulated p53 gene signature but not the p53-wildtype signature. Enrichment of the 'p53-dysregulation' signature suggests that these genes are also involved in normal p53 developmental patterns due to the decreased p53 pathway activity seen in developing fetal salivary tissues (Fig. 1F and Supplementary Fig. S2C). Thus, regulation of the p53 pathway during normal salivary gland development is more similar to that observed in p53-mutant tumor cells with pathway dysregulation. We next examined these p53 signatures across samples and found that, like fetal samples, high-grade MEC tumors display an increase in the p53 dysregulation signature ($P < 0.001$) compared to low-grade MEC and normal adult samples (Fig. 2F, G). Upon examining MEC tumors stratified by C1/M2 status alone, we confirmed that MDM2 levels are significantly higher in C1/M2-positive tumors compared to normal adult and fetal samples (Supplementary Fig. S2D). These results support a role for MDM2-mediated p53 loss in driving pathway dysregulation as a common feature of C1/M2-positive salivary MEC progression.

Combined C1/M2 fusion expression and Trp53 loss in murine salivary gland ducts drives histologically advanced MEC

To investigate the role of transcriptional programs operational in fetal development that may drive salivary MEC progression in vivo,

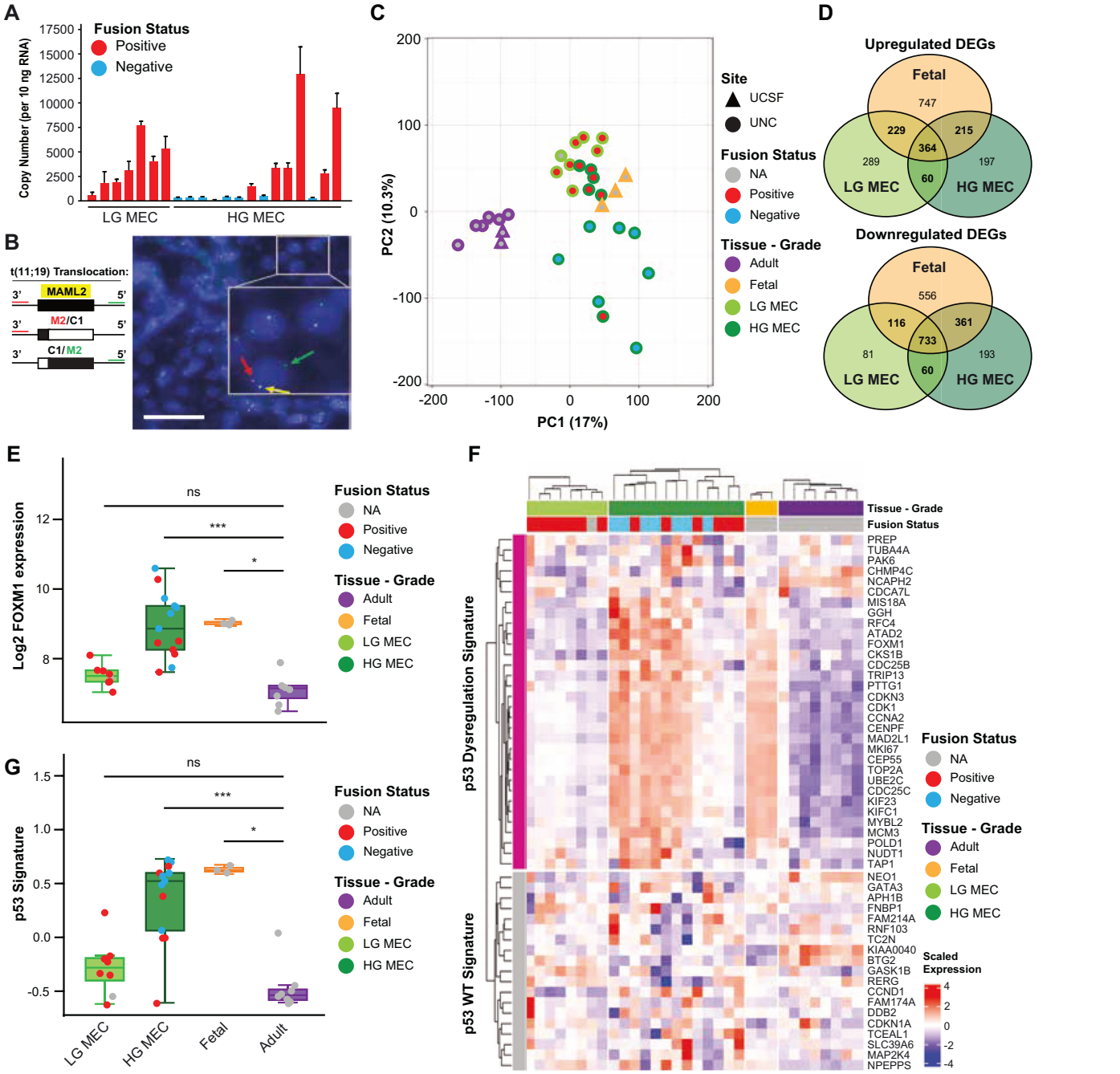

we next sought to generate a genetically engineered mouse model (GEMM) of salivary MEC. The CRTC1 promoter, which drives expression of C1/M2 in MEC cells harboring the t(11;19) translocation, is active within submandibular gland epithelia during early stages of salivary gland development [66]. This promoter activity disappears during gland differentiation and maturation but is reactivated with the onset of tumorigenesis [66]. This stage-dependent expression pattern supports a role in embryonic branching morphogenesis but not acinar differentiation, suggesting that salivary MEC arises from progenitor cells located within the salivary glands [26, 67–69]. Thus, we designed several GEMMs using an established *C1/M2* transgenic and targeted oncogene expression to putative progenitor cell types located within the salivary gland [20]. Prior studies suggested that the salivary acini may be maintained by self-duplication of Mist1-positive cells, while the salivary ducts and myoepithelial cells are maintained by Krt14-positive cells, with additional contributions to intercalated duct maintenance potentially coming from Dcpp1-positive cells [47, 68, 70, 71]. These studies suggested that these multipotent cell populations could give rise to the heterogeneous phenotype observed in salivary MEC. Thus, to achieve selective and inducible C1/M2 expression within specific salivary gland progenitor cell types, we employed crosses to *Mist1-CreER* [71], *Dcpp1-CreER* [47], and *KRT14-CreER* [72] strains to drive tamoxifen-inducible *Cre* recombinase expression within acinar cells, intercalated ductal/serous demilune cells, or myoepithelial and basal ductal epithelial cells, respectively. Administration of tamoxifen to 8-week-old animals promoted Cre-mediated excision of LoxP-STOP-LoxP cassettes, leading to expression of C1/M2 and a LumiFluor bioluminescent reporter [49] (Fig. 3A, B).

Fig. 2 High-grade salivary MEC tumors and developing fetal salivary glands are characterized by dysregulation of the p53 pathway. **A** qPCR analysis of *C1/M2* expression in low-grade and high-grade human MEC tumor samples. *C1/M2* copy number per 10 ng input RNA was calculated based on a standard curve. Samples with ≥500 copies of C1/M2 per 10 ng input RNA were considered C1/M2-positive. Data is presented as the mean ± SD ($n = 3$ minimum technical replicates), excluding human MEC tumor samples where C1/M2 copy number was undetermined. **B** *Left*, the red and green fluorescent probes of the ZytoLight MAML2 Dual Color Break Apart Probe bind to the 3′ and 5′ ends of the MAML2 gene, respectively. *Right*, break apart MAML2 FISH showing a rearrangement involving MAML2 in a representative high grade MEC sample. Red and green arrows indicate location of single probe binding, with yellow arrow showing probe colocalization. Scale bar, 200 μm. **C** Principal component analysis of all parotid samples organized by collection site (UNC or UCSF), *C1/M2* fusion status, and tissue origin and grade. **D** Venn diagrams showing the total number of overlapping DEGs in MEC tumors by grade number of upregulated (logFC ≥2.00) and downregulated (logFC ≤−2.00) genes. Genes altered in low-grade MEC, high-grade MEC, and fetal tissue are shown in the green, dark green, and yellow circles, respectively. The upper Venn diagram shows overlapping upregulated genes and the lower Venn diagram shows overlapping downregulated genes. **E** Log2 normalized counts of FOXM1 data generated via RNAseq. In the box and whisker plot, the horizontal line within the box represents the median, and the whiskers extend to ±1.5x the interquartile range (1.5*IQR). Wilcoxon-rank sum test of pairwise comparisons: ***$P < 0.001$; *$P < 0.05$; ns, not significant ($P > 0.05$). **F** Supervised cluster analysis of MEC tumor samples, adult salivary glands, and fetal salivary glands using the Troester et al. [98] 52-gene p53 signature. The fold change relative to the median expression value across all tumors is shown. The dendrogram branch is enriched for p53 mutant or p53 wild-type signatures (shown in magenta and gray, respectively). **G** Spearman correlation calculated for the Troester et al. [98] p53 signature (a composite of the wild-type and dysregulated signatures shown in panel **F**) in low-grade MEC (light green), high-grade MEC (dark green), fetal salivary tissue (yellow), and adult salivary tissue (purple). In the box and whisker plot, the horizontal line within the box represents the median, and the whiskers extend to ±1.5*IQR. Wilcoxon-rank sum test of pairwise comparisons: ***$P < 0.001$; *$P < 0.05$; ns, not significant ($P > 0.05$). DEG differentially expressed gene, FC fold change, C1/M2 CRTC1-MAML2, FOXM1 forkhead box protein M1, GSVA gene set variation analysis, HG high-grade, LG low-grade, MEC mucoepidermoid carcinoma, NES normalized enrichment score, ns not significant, PC1 principal component 1, PC2 principal component 2, qPCR quantitative polymerase chain reaction, RNAseq RNA sequencing, UCSF University of California at San Francisco, UNC University of North Carolina.

Bioluminescent imaging of these GEMMs at several time points following tamoxifen injection revealed sustained LumiFluor signal in the salivary region of *Mist1-CreER;LumiFluor* and *KRT14-CreER;LumiFluor* animals but no detectable LumiFluor signal in control or *Dcpp1-CreER;LumiFluor* animals (Fig. 3B). Analysis of the murine major salivary glands by qPCR revealed conditional *C1/M2* gene expression in the submandibular, sublingual, and parotid glands of *Dcpp1-CreER;C1/M2* mice (Fig. 3C). C1/M2 expression was primarily observed in the submandibular glands (Fig. 3C). In contrast, comparatively low expression was observed in another exocrine gland tissue (Supplementary Fig. S3A). Despite *C1/M2* expression within the tissues of interest, these animals did not develop MEC tumors within 18 months following tamoxifen administration (Supplementary Fig. S3B). However, histological analysis of submandibular glands from each of these GEMM animals revealed several abnormalities including hypergranularity of the striated ducts in the *Dcpp1-CreER;C1/M2 and Mist1-CreER;C1/M2* mice and depletion of the acinar cell population in the acini of *Dcpp1-CreER;C1/M2 and Mist1-CreER;C1/M2* mice. Notably, dramatic disorganization of both acinar and ductal structures was observed in *KRT14-CreER;C1/M2* mice, suggesting a role for these cells in salivary MEC pathogenesis (Fig. 3D and Supplementary Table S2).

To test whether the observed p53 dysregulation is indeed involved in MEC pathogenesis, we next generated a GEMM in which *KRT14*-driven *CreER* expression drives conditional and inducible *Trp53* (transformation related protein 53) loss (heterozygous loss, $Trp53^{fl/+}$; homozygous loss, $Trp53^{fl/fl}$) along with simultaneous *C1/M2* and *LumiFluor* reporter expression within basal ductal epithelial cells (Fig. 4A). Several *KRT14-CreER;LumiFluor;C1/M2;*$Trp53^{fl/fl}$($KLCT^{fl/fl}$) animals developed autochthonous salivary gland tumors with delineated features arising from within the submandibular glands compared to adjacent normal tissue (Fig. 4B and Supplementary Table S2). Tumors became palpable between 4 and 6 months following tamoxifen administration (mean tumor latency time, 145.8 days) with animals quickly reaching endpoint within 1 to 2 weeks after the appearance of a palpable masses. Analysis of C1/M2 copy number in these murine tumors revealed similar C1/M2 expression to that exhibited by human MEC samples (Fig. 4C). While only animals with *C1/M2* expression and combined homozygous *Trp53* loss developed salivary tumors, littermate controls, including those with heterozygous *Trp53* loss ($Trp53^{fl/+}$) were also generated for investigation. Several of these other genotypes reached endpoint within approximately 1 to 2 years of tamoxifen administration due to a variety of off-target effects including perioral and cutaneous pilosebaceous cysts (Fig. 4D and Supplementary Figure S4A–E). Despite appearance of several premalignant histologic abnormalities, animals with heterozygous *Trp53* loss ($KLCT^{fl/+}$) did not develop salivary tumors even though LumiFluor signal within the submandibular gland was detected at levels comparable to that observed in animals with homozygous *Trp53* loss ($KLCT^{fl/fl}$) (Fig. 4E).

Murine tumor histology was graded by two independent oral pathologists according to the Armed Forces Institute of Pathology [28], Brandwein [27], and Memorial Sloan Kettering Cancer Center [29] grading systems. Notably, the autochthonous murine salivary gland tumors displayed multiple characteristics commonly associated with high-grade human MEC, including an intracystic component of <20% and >4 mitoses per 2 mm^2 tumor area (Table 2). Nearly all tumors exhibited necrosis, anaplasia, and tumor invasion into small nests and islands and no tumors exhibited perineural or bone invasion. Murine tumors were focally positive for periodic acid Schiff (PAS) and mucicarmine staining, indicating the presence of mucin, which is characteristic of MEC (Table 2, Fig. 4F and Supplementary Fig. S4F). Immunohistochemical analyses of known molecular hallmarks of human MEC were performed on tumor sections, confirming activation of pro-growth signaling with p-AKT (S473) and p-ERK1/2 (T202/Y204), cell proliferation with Ki-67, and induction of apoptosis with cleaved caspase-3 compared to control tissues (Fig. 4G and Supplementary Fig. S4G). Control submandibular glands and murine MEC tumors were compared using H-score quantification of the immunohistochemical staining, revealing elevated p-AKT (S473) and Ki-67 expression (G1-S cell cycle marker) in the murine MEC tumors relative to the control glands (Fig. 4H and Supplementary Fig. S4H). Finally, bulk RNAseq was used to compare murine MEC tumors, human fetal salivary glands, and high- and low-grade human MEC tumors. We identified DEGs from murine MEC tumors relative to normal murine salivary gland controls, human fetal salivary glands relative to human adult normal salivary glands, and low- or high-grade salivary MEC tumors relative to adult normal salivary glands. Remarkably, murine MEC tumors share a larger number of unique DEGs with human fetal salivary samples and high-grade human MEC samples (187 genes) than with fetal samples and low-grade human MEC samples (82 genes; Fig. 4I and Supplementary Table S1). These findings establish the $KLCT^{fl/fl}$ genetically engineered mouse model as a bona fide model of

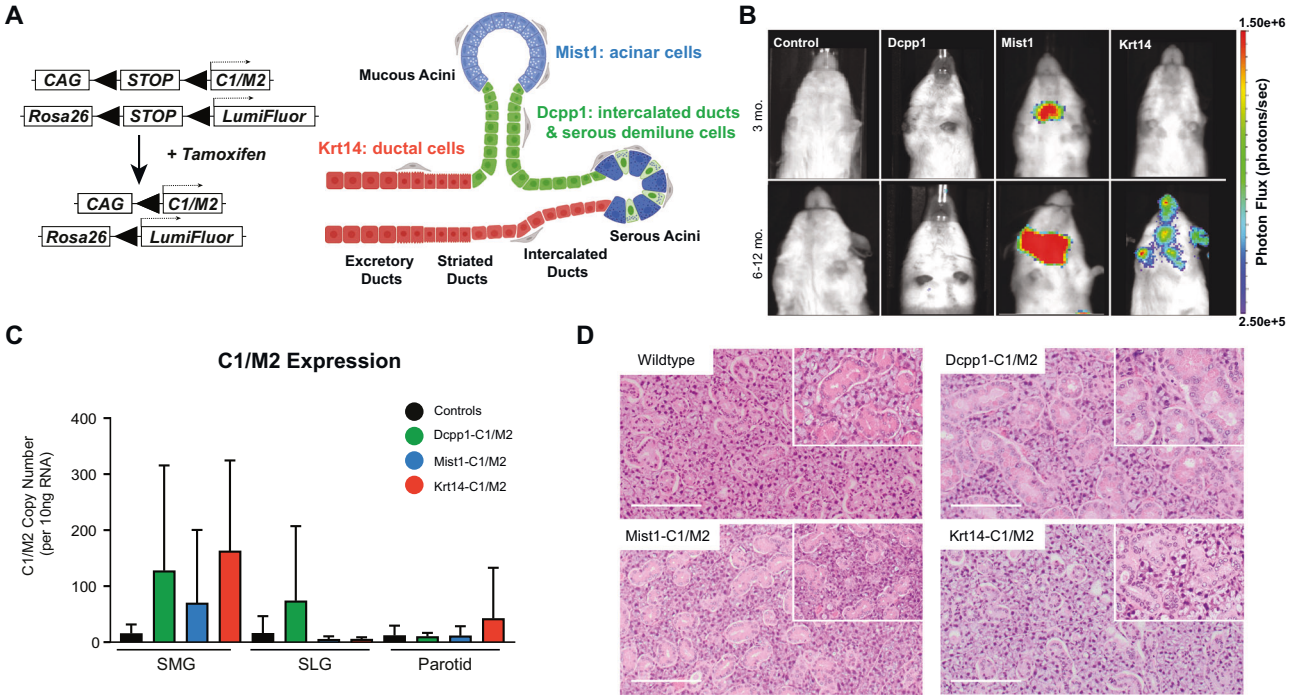

Fig. 3 Cell type-specific targeting of CRTC1-MAML2 to murine salivary glands identifies Krt14-positive basal epithelial progenitors that drive early ductal pathogenesis. A Schematic representation of CreER/LoxP-mediated *C1/M2* transgene expression in salivary glands. *Left*, Injection of transgenic animals with tamoxifen results in CreER activation, elimination of the STOP cassette, and subsequent expression of *C1/M2* and the LumiFluor reporter in target cells. *Right*, The KRT14 promoter was used to express CreER in all salivary ductal cells, including the excretory, striated, and intercalated ductal cells, and myoepithelial cells. The Mist1 promoter was used to express CreER in all salivary acinar cells, including serous and mucous acinar cells. The Dcpp1 promoter was used to express CreER in the salivary intercalated ductal cells and the serous demilune cells. **B** Representative BLI images of control (*LumiFluor* allele with no CreER driver allele), *Dcpp1-CreER;LumiFluor*, *Mist1-CreER;LumiFluor*, and *KRT14-CreER;LumiFluor* animals 3 months and 6 to 12 months post-tamoxifen treatment. The scale bar indicates photons/sec. **C** qPCR analysis of *C1/M2* expression in control (*C1/M2*-negative) ($n = 8$), *Dcpp1-CreER;C1/M2* ($n = 10$), *Mist1-CreER;C1/M2* ($n = 4$), and *KRT14-CreER;C1/M2* ($n = 4$) animals up to 13 months post tamoxifen administration. *C1/M2* transcript copy number per 10 ng input RNA was calculated based on a standard curve. Data is presented as the mean ± SD. **D** Representative H&E-stained submandibular glands from control (*Mist1-CreER* only), *Dcpp1-CreER;C1/M2*, *Mist1-CreER;C1/M2*, and *KRT14-CreER;C1/M2* animals 6–9 months post tamoxifen administration. Scale bar indicates 200 µm at ×10 ×10 magnification. Inset images reflect ×60 ×10 magnification. BLI bioluminescent imaging, qPCR quantitative polymerase chain reaction, SLG sublingual gland, SMG submandibular gland.

advanced salivary MEC suitable for investigating the mechanisms involved in tumor progression.

Pro-tumorigenic FGFR2 alternative splicing is characteristic of high-grade MEC

To understand the potential transcriptional programs that uniquely regulate salivary MEC tumorigenesis compared to normal fetal salivary gland development, we analyzed DEGs according to tumor grade and identified members of the fibroblast growth factor ligand/receptor (FGF/FGFR) family that were differentially expressed in fetal tissues or MEC tumors compared to adult normal salivary glands (Fig. 5A). FGFR and FGF signaling ligands are regulators of branching morphogenesis during development of multiple exocrine organs, including the salivary glands [73–80]. Bioinformatics analyses revealed that FGF10, which is an activating ligand of the specific FGFR splice isoforms that induce salivary epithelial cell differentiation (i.e., FGFR2b) [74, 81, 82], is significantly downregulated in human high-grade MEC (FC = −1.97, $P < 0.05$; Fig. 5A and Supplementary Fig. S5) relative to human adult normal salivary glands and GEMM tumors relative to murine adult normal salivary glands (FC = −3.28, $P < 0.05$; Supplementary Table S1). In addition, Reactome pathway analysis showed that FGFR2b Ligand Binding and Activation pathway is significantly downregulated (NES = −1.639, $P < 0.05$) in human high-grade MEC relative to normal adult salivary glands (Fig. 5B and Supplementary Fig. S6A–C).

Post-transcriptional regulation of FGFR2 determines its function whereby alternative splicing generates either an FGFR2b or FGFR2c isoform (Supplementary Fig. S10A). While the FGFR2b variant drives salivary gland differentiation and apoptosis and acts as a tumor suppressor [83], the FGFR2c variant drives epithelial-to-mesenchymal transition leading to disease progression in many cancers [84]. Mutually exclusive splicing of exons 8 and 9 in the ligand-binding domain of FGFR2 produces these two frequently expressed isoforms, FGFR2b and FGFR2c [84]. This alternative splicing event occurs within the third immunoglobulin loop region and thus regulates extracellular ligand selectivity [84]. Consequently, FGFR2b and FGFR2c variants have distinct effects on regulating proliferation, glandular development, and apoptosis. Although there are substantial similarities between the transcriptional signatures of fetal development and MEC tumorigenesis, the C1/M2 fusion oncogene is a defining feature of MEC pathogenesis and has been implicated in regulating co-transcriptional splicing [85]. This led us to further examine the differences in FGFR2 splice variant expression according to different salivary MEC grades.

Visualization of RNAseq data using the UCSC genome browser revealed that adult and fetal salivary gland tissues exhibit similar FGFR2 exon 8 inclusion, but high-grade and low-grade MEC display a dramatic decrease in exon 8 inclusion corresponding to the FGFR2b isoform (Fig. 5C and Supplementary Fig. S7–S9). Quantification of differential alternative splicing by rMATS confirmed a decrease in the exon 8 inclusion levels (PSI, Ψ) within C1/M2-positive low-grade and high-grade salivary MEC samples (Fig. 5D). In contrast, there is an increase in exon 9 inclusion corresponding to the FGFR2c isoform accompanied by upregulation of the FGFR2c

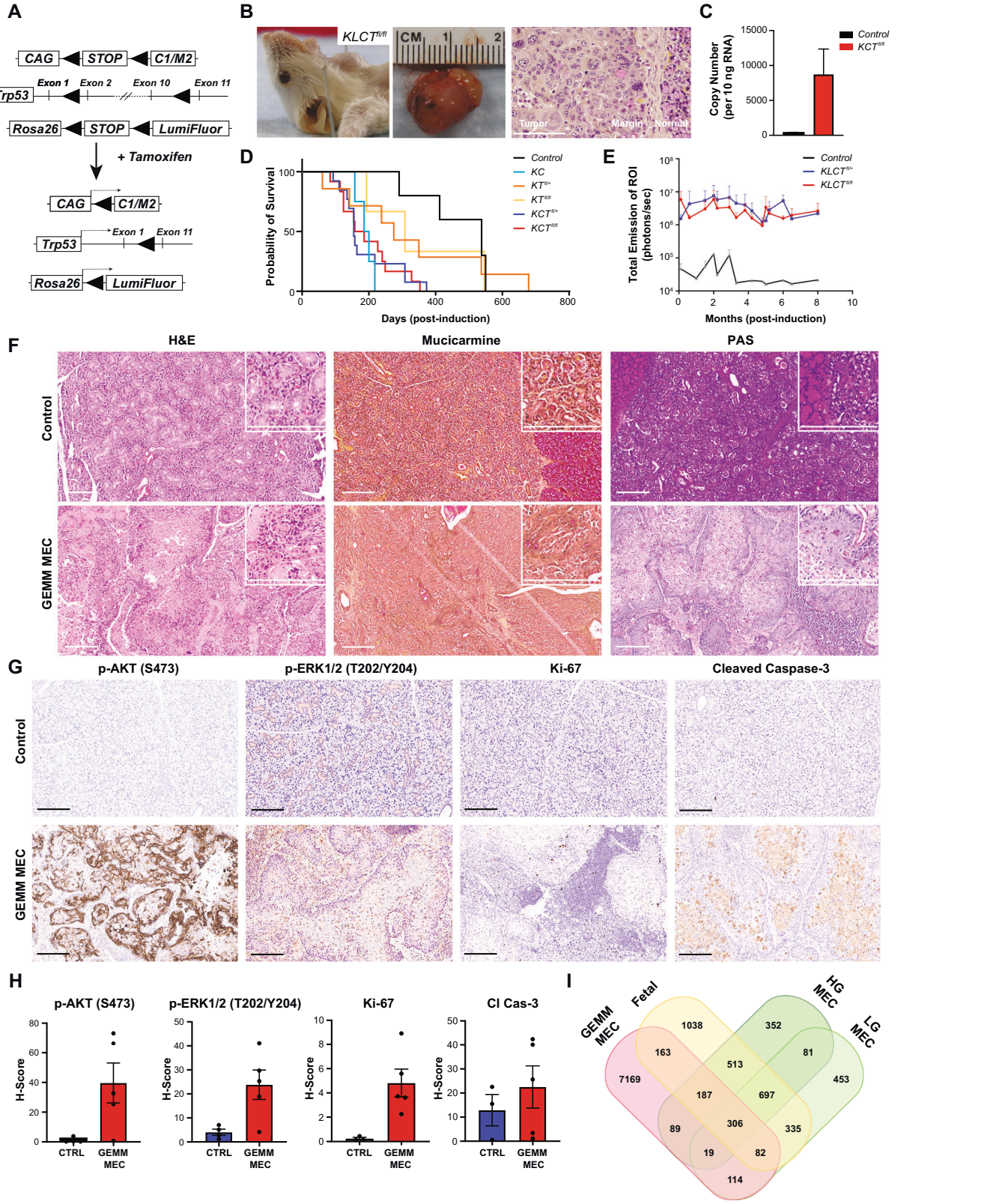

ligands FGF5, FGF16, and FGF18 (Fig. 5C and Supplementary Fig. S5). These results implicate a differential FGFR signaling axis in salivary MEC pathogenesis that is mediated by alternative splicing to promote expression of the pro-tumorigenic FGFR2c isoform. To validate these findings, we examined *Fgfr2* alternative splicing in our autochthonous $KLCT^{fl/fl}$ GEMM MEC model using exon junction-spanning qPCR primers designed to selectively detect *FGFR2b* versus *FGFR2c* (Supplementary Fig. S10B). GEMM MEC tumors express significantly higher ($P < 0.001$) levels of FGFR2c relative to control littermate tissues while FGFR2b expression is not significantly

Fig. 4 Dysregulation of p53 cooperates with C1/M2 to promote formation of tumors that share phenotypic hallmarks of human high-grade MEC. A Schematic representation of *KRT14-CreER/LoxP*-mediated *C1/M2* transgene expression coupled with *Trp53* loss. **B** *Left*, representative *KRT14-CreER;C1/M2;LumiFluor;Trp53*$^{fl/fl}$ mouse that developed a salivary gland tumor. *Middle*, the resected salivary gland tumor. *Right*, representative mucicarmine-stained tumor section. A defined border separates tumor tissue (left) from adjacent normal tissue (right). **C** qPCR analysis of *C1/M2* expression in control ($n = 8$) and *KRT14-CreER; LumiFluor;Trp53*$^{fl/fl}$ (*KCT*$^{fl/fl}$; $n = 3$) GEMM MEC tumor samples. *C1/M2* copy number per 10 ng input RNA was calculated based on a standard curve. Data is presented as the mean ± SEM ($n = 4$ minimum technical replicates). **D** Overall survival of control ($n = 5$), *KRT14-CreER;C1/M2* (*KC*; $n = 4$), *KRT14-CreER;Trp53*$^{fl/fl}$ (*KT*$^{fl/fl}$; $n = 3$), *KRT14-CreER;Trp53*$^{fl/+}$ (*KT*$^{fl/+}$; $n = 10$), *KRT14-CreER;C1/M2;Trp53*$^{fl/+}$ (*KCT*$^{fl/+}$; $n = 13$), and *KRT14-CreER;C1/M2;Trp53*$^{fl/fl}$ (*KCT*$^{fl/fl}$; $n = 12$) animals. **E** Quantification of total bioluminescent emission (photons/sec) from the salivary gland region in *KRT14-CreER;LumiFluor;C1/M2;Trp53*$^{fl/+}$ (*KLCT*$^{fl/+}$; $n = 7$), *KRT14-CreER;LumiFluor;C1/M2;Trp53*$^{fl/fl}$ (*KLCT*$^{fl/fl}$; $n = 10$), and control (no *KRT14-CreER* allele; $n = 3$) animals, plotted as months post-tamoxifen induction. **F** Representative H&E-stained images of a control (*LumiFluor;C1/M2*) submandibular gland and a *KRT14-CreER;C1/M2;Trp53*$^{fl/fl}$ MEC tumor. Scale bar: 200 μm. **G** Representative stained images from a control (*LumiFluor;C1/M2*) submandibular gland and a *KRT14-CreER;C1/M2;Trp53*$^{fl/fl}$ MEC tumor. IHC staining was performed for p-AKT (S473), p-ERK1/2 (T202/Y204), Ki-67, and cleaved caspase-3. Scale bar: 200 μm. **H** Quantification of IHC H-scores in panel G. Data is presented as the mean ± SEM. **I** Venn diagram showing a comparison of DEGs captured by RNAseq of GEMM MEC tumors compared with human fetal salivary glands and low-grade and high-grade MEC tumors. BLI bioluminescent imaging, Cl Cas-3 cleaved caspase-3, CTRL control animals, DEG differentially expressed gene, GEMM genetically engineered mouse model, IHC immunohistochemistry, MEC mucoepidermoid carcinoma, PAS periodic acid-Schiff, qPCR quantitative polymerase chain reaction, RNAseq RNA sequencing.

Table 2. Histological characteristics and grading of murine salivary MEC-like tumors.

	mT1	mT2	mT3	mT4	mT5
Sex	M	F	F	M	M
Tumor location	SMG	SMG	SMG	SMG	Salivary, possibly parotid
Intracystic <20%	Yes	Yes	Yes	Yes	Yes
PNI	No	No	No	No	N/A
Mitoses (per 2 mm^2)	>4	>4	>4	>4	>4
Necrosis	Yes	Yes	Yes	No	Yes
Anaplasia	Yes	Yes	Yes	No (mild)	Yes
Small nest	Yes	Yes	Yes	No	N/A
Border	Infiltrative	Infiltrative	Infiltrative	Well-circumscribed	N/A
LVI	Yes	No	No	No	N/A
Bone invasion	No	No	No	No	N/A
Cell components	Epidermoid	Squamous with keratinization»epidermoid cells>clear cells>mucocytes	Oncocytic cells»epidermoid cells>mucocytes	Epidermoid (spindly)»squamous with keratinization>ductal structures>mucocytes	Squamous with keratinization
Mucicarmine	Negative	Negative	Focally positive	Focally positive	Negative
PAS	Focally positive	Focally positive	Focally positive	Focally positive	Focally Positive
RNAseq run	Yes	Yes	Yes	Yes	No
AFIP grade[a]	High	High	High	Intermediate	High
Brandwein grade[b]	High	High	High	High	High
MSKCC grade[c]	High	High	High	High	High

[a]The AFIP scoring system [28] is a point-based system in which specific tumor histologic parameters are assigned a point value and higher scores correspond to higher tumor grades. The following histologic parameters are included in the AFIP scoring system: intracystic component <20%, perineural invasion, necrosis, mitoses (>4 per high-powered field), and anaplasia/nuclear atypia. Higher overall scores correspond to higher tumor grades.
[b]The Brandwein scoring system [27] is a point-based system in which specific tumor histologic parameters are assigned a point value and higher scores correspond to higher tumor grades. The following histologic parameters are included in the Brandwein scoring system: intracystic component <25%, perineural invasion, necrosis, mitoses (>4 per high-powered field), anaplasia/nuclear atypia, pattern of infiltration (nests/islands), angiolymphatic invasion, and bone invasion.
[c]The MSK grading system [29] is a qualitative grading system that takes into account the following histologic parameters: intracystic component, necrosis, mitoses, anaplasia/nuclear atypia, and pattern of infiltration.
AFIP, Armed Forces Institute of Pathology; F, female; LVI, lymphovascular invasion; M, male; MSKCC, Memorial Sloan-Kettering Cancer Center; mT, murine tumor; PAS, Periodic acid-Schiff [stain]; PNI, perineural invasion; RNAseq, RNA sequencing; SMG, submaxillary gland.

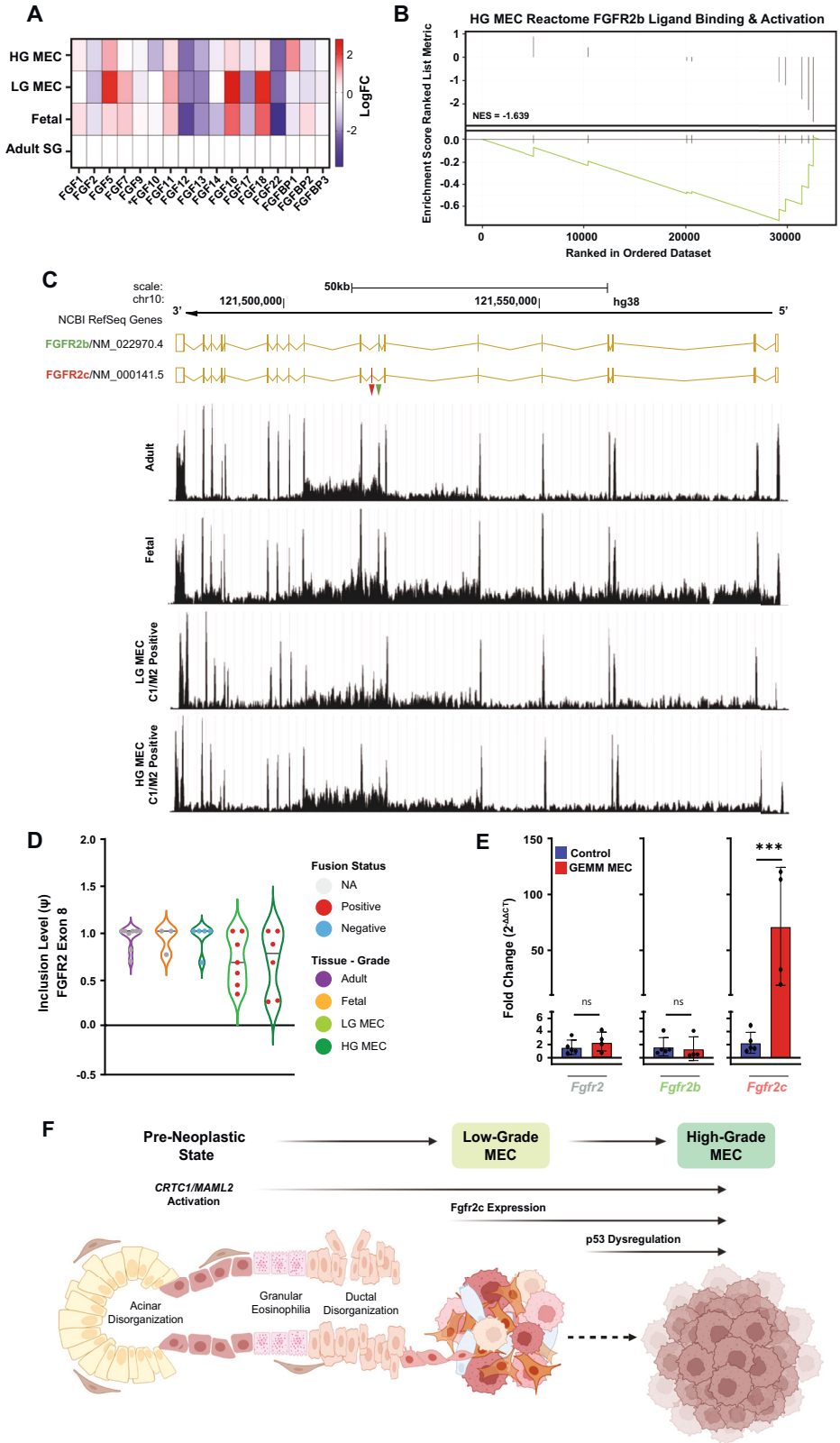

different (Fig. 5E). Collectively, these findings implicate corruption of transcriptional programs that mediate fetal salivary gland development and regeneration in the pathogenesis of salivary MEC via alterations in pro-tumorigenic FGFR2c signaling within Krt14-positive basal epithelial cells (Fig. 5F).

DISCUSSION

In this study, transcriptomic profiling analyses revealed that MEC tumors and fetal salivary glands display overlapping gene expression profiles that are involved in proliferation and developmental signaling and linked to p53 dysregulation. We show that

Fig. 5 Alternative FGFR2 isoform usage establishes a pro-tumorigenic pathway in salivary MEC versus normal salivary glands. A LogFC expression of FGF ligand and FGFR family members in human fetal salivary glands, low-grade MEC tumors, and high-grade MEC tumors compared to adult salivary gland tissue. **B** FGFR2b Reactome pathway analysis of high-grade MEC tumors. **C** *Above*, annotated illustration of the NCBI RefSeq gene reference for the two primary FGFR2 isoforms, curated subset (NM_* Annotation release 13 July 2013). *Below*, representative cigar plots of RNAseq data for FGFR2 visualized using the UCSC Genome Browser from adult salivary glands, fetal salivary glands, C1/M2-positive low-grade MEC tumors, and C1/M2 positive high-grade (HG) MEC tumors. **D** Quantification of FGFR2 exon 8 Percent Spliced In (PSI; Ψ) inclusion levels calculated by rMATS. Data represented as a violin plot with the mean as solid horizontal line and extending to the minimum and maximum values. **E** qPCR analysis of FGFR2 splice isoform expression in control and GEMM MEC tissues. ***$P < 0.001$; ns, not significant ($P > 0.05$). **F** Graphical schematic of proposed MEC progression cascade. The preneoplastic state is characterized by acinar disorganization, granular eosinophilia, and ductal disorganization upon acquisition of the t(11;19) translocation and C1/M2 expression. During the course of MEC oncogenesis, a shift in Fgfr2 isoform expression from the epithelial type, Fgfr2b, to a more mesenchymal form, Fgfrc marks the transition from a preneoplastic state to low-grade MEC. This receptor isoform switch is maintained in progression from low-grade to high-grade which is further characterized by p53 dysregulation, which we observed to be a feature shared with developing fetal salivary gland tissues. Generated using Biorender software. FC fold change, FGF fibroblast growth factor, FGFR fibroblast growth factor receptor, GEMM genetically engineered mouse model, HG high-grade, IgIII immune-globulin III domain, KD kinase domain, LG low-grade, MEC mucoepidermoid carcinoma, NES normalized enrichment score, Padj adjusted *P* value, qPCR quantitative polymerase chain reaction, RNAseq RNA sequencing, SG salivary gland, TM transmembrane domain.

combined overexpression of the strong transcriptional coregulator fusion C1/M2 and dysregulation of the p53 pathway promotes developmental programs that induce formation of advanced salivary MEC. Interestingly, p53 is frequently wild-type in salivary MEC but may be transcriptionally repressed and/or targeted for degradation by overexpression of MDM2, leading to p53 pathway dysregulation [63]. Using this information, we engineered the first GEMM of advanced, high-grade MEC by selectively targeting several distinct cell types that are known or predicted to possess pluripotent characteristics important for driving salivary gland development. Specifically, we demonstrated that salivary ductal epithelial cells are involved in salivary MEC tumorigenesis by targeting conditional and inducible *Trp53* loss along with *C1/M2* fusion oncogene expression in Krt14-positive basal epithelial cells of the salivary gland ducts.

The development of in vivo models that can recapitulate the pathobiology of high grade MEC is crucial for understanding disease progression and testing potential therapeutic strategies. Previous attempts at modeling MEC have utilized the mouse mammary tumor virus (MMTV) promoter to drive *C1/M2* expression [20]. However, while this model is fully penetrant, tumors are phenotypically low-grade and this targeting strategy activates *C1/M2* oncogene expression within multiple cell types in other secretory glands, including mammary tissues [86]. In contrast, our GEMM addresses an urgent need in the field to define the mechanisms governing salivary MEC progression by providing a model that recapitulates both the molecular and the phenotypically dedifferentiated features characteristic of advanced, high-grade disease. Our approach of targeting *C1/M2* expression specifically to Krt14-positive ductal cells in the murine salivary gland yielded tumors that recapitulate the gene expression profiles and histological features of human high-grade salivary MEC. The success of this approach is supported by evidence that Krt14-positive salivary gland cells are slow-cycling multipotent progenitor cells that proliferate in response to injury, contribute to regeneration and can differentiate into multiple salivary gland cell types [68, 70, 87–89]. Extrapolating these findings to MEC, Krt14-positive cells expressing the C1/M2 oncogene may be able to rapidly proliferate to form a tumor composed of the variety of cell types characteristic of MEC tumors as compared to Mist1- positive or the rare Dcpp1-positive cells which may represent cell types with minimal or reduced multi-potency potential.

Our autochthonous GEMM provides mechanistic insights into the role of p53 in salivary MEC progression and offers an opportunity to explore the benefits of therapeutics targeting the p53 pathway. This has opened the door to p53-activating therapeutics, such as the MDM2 inhibitor MI-773, in the clinical management of this disease [64, 65]. p53 is a well-known tumor suppressor which functions to suppress proliferation signals [90–92]. While some *TP53* gene alterations have been previously detected in MEC, they are infrequent compared to other cancers and appear to be mutually exclusive to the t(11;19) translocation and C1/M2 fusion expression in MEC [92, 93]. However, the bioinformatics analyses performed in this study reveal that developing fetal salivary glands and high-grade MEC share similar p53 pathway regulation which leads to higher expression of pro-proliferation signaling molecules, such as FOXM1. In contrast, low-grade MEC do not share this same level of p53 pathway regulation. While C1/M2-positive salivary MEC tumors harbor wild-type p53, we observe progressive elevation of *MDM2* according to tumor grade, suggesting that post-translational loss of p53 drives disease progression. Consequently, the work presented herein supports a role for C1/M2 as the earliest etiologic event driving MEC tumorigenesis and indicates that p53 dysregulation provides a previously unreported molecular switch that contributes to tumor progression from low-grade to high-grade disease. Despite innovative therapies such as MI-773 being explored for their potential utility in p53 wild-type salivary cancers [64], the identification of additional potential therapeutic vulnerabilities is urgently needed for patients with advanced salivary MEC.

To understand the potential mechanistic determinants that govern normal salivary gland development versus salivary MEC tumorigenesis, we extended our transcriptomic analyses to include computational analysis of alternative transcript splicing. Surprisingly, expression of the tumor suppressive FGFR2b isoform and the pro-tumorigenic FGFR2c isoform is altered between fetal salivary gland tissues and salivary MEC. FGFR inhibitors have recently gained FDA approval as targeted agents for use in a variety of different cancers. These therapeutics include pan-FGFR inhibitors (e.g., erdafitinib), receptor-specific inhibitors (e.g., FGFR2; pemigatinib), or inhibitors that target FGFR fusions/rearrangements (e.g., futibatinib) [94]. Unfortunately these strategies currently lack the ability to target specific FGF receptor isoforms arising from alternative splicing. However, in vitro studies using antisense oligonucleotides to restore FGFR2b isoform signaling have shown promising results in resensitizing prostate cancer cell lines to chemotherapy [95] and radiotherapy [96]. Our findings in salivary MEC underscore the potential for developing novel approaches against tumorigenic alternative splicing and serve as a new frontier for targeted therapeutic strategies for MEC. Taken together, these results implicate an FGFR-p53 developmental signaling axis in MEC progression and suggest a role for selective FGFR targeting therapies in the treatment of high-grade MEC.

Limitations of the study

Relative to all cancers, the incidence of salivary MEC is rare. As such, the accrual of MEC samples, especially high-grade cases, as well as fetal tissues to this study was limited. Though salivary gland tumors

were successfully generated in our MEC GEMM, one limitation of the model is its low penetrance. Only a small fraction of the *KRT14-CreER;C1/M2;Trp53*$^{fl/fl}$ mice included in this study developed salivary tumors (approximately 15%). A larger proportion of mice were sacrificed at early time points due to off-target effects such as severe cystic pathology of pilosebaceous origin exhibited in the skin of the muzzle, paws, tail, and genital regions, and it is likely that these animals would have also developed salivary tumors had they been allowed to continue in the study. To increase the specificity of Cre activation and mitigate off-target effects in this model, targeted delivery of tamoxifen may vastly improve tumor penetrance. A previous study demonstrated the use of ductal cannulation to achieve local delivery of nanomaterials to the murine submandibular gland [97]. Future studies will explore this procedure to realize the full potential of the GEMM described here.

DATA AVAILABILITY

The datasets generated during and/or analyzed during the current study are available in the NCBI Gene Expression Omnibus repository. The normalized gene expression data matrices and clinical annotation for this study are available at the Gene Expression Omnibus under GSE143702 and GSE282430.

CODE AVAILABILITY

All computer code employed are commercially available. No custom computer code was generated or used for the analyses performed in this study.

REFERENCES

1. Lee MY. Embryonic programs in cancer and metastasis-insights from the mammary gland. Front Cell Dev Biol. 2022;10:938625.
2. Coghe F, Fanni D, Gerosa C, Ravarino A, Mureddu M, Cerrone G, et al. The role of fetal programming in human carcinogenesis - may the Barker hypothesis explain interindividual variability in susceptibility to cancer insurgence and progression?. Eur Rev Med Pharm Sci. 2022;26:3585–92.
3. Balachandran S, Narendran A. The developmental origins of cancer: a review of the genes expressed in embryonic cells with implications for tumorigenesis. Genes. 2023;14:604.
4. Meacham CE, Morrison SJ. Tumour heterogeneity and cancer cell plasticity. Nature. 2013;501:328–37.
5. Junttila MR, de Sauvage FJ. Influence of tumour micro-environment heterogeneity on therapeutic response. Nature. 2013;501:346–54.
6. Stanta G, Bonin S. Overview on clinical relevance of intra-tumor heterogeneity. Front Med (Lausanne). 2018;5:85.
7. Dentro SC, Leshchiner I, Haase K, Tarabichi M, Wintersinger J, Deshwar AG, et al. Characterizing genetic intra-tumor heterogeneity across 2,658 human cancer genomes. Cell. 2021;184:2239–54.
8. Marusyk A, Janiszewska M, Polyak K. Intratumor heterogeneity: the Rosetta Stone of therapy resistance. Cancer Cell. 2020;37:471–84.
9. Gavish A, Tyler M, Greenwald AC, Hoefflin R, Simkin D, Tschernichovsky R, et al. Hallmarks of transcriptional intratumour heterogeneity across a thousand tumours. Nature. 2023;618:598–606.
10. Bleckmann SC, Blendy JA, Rudolph D, Monaghan AP, Schmid W, Schütz G. Activating transcription factor 1 and CREB are important for cell survival during early mouse development. Mol Cell Biol. 2002;22:1919–25.
11. Struthers RS, Vale WW, Arias C, Sawchenko PE, Montminy MR. Somatotroph hypoplasia and dwarfism in transgenic mice expressing a non-phosphorylatable CREB mutant. Nature. 1991;350:622–4.
12. Rosenberg D, Groussin L, Jullian E, Perlemoine K, Bertagna X, Bertherat J. Role of the PKA-regulated transcription factor CREB in development and tumorigenesis of endocrine tissues. Ann N Y Acad Sci. 2002;968:65–74.
13. Sundaram N, Tao Q, Wylie C, Heasman J. The role of maternal CREB in early embryogenesis of Xenopus laevis. Dev Biol. 2003;261:337–52.
14. Sakamoto KM, Frank DA. CREB in the pathophysiology of cancer: implications for targeting transcription factors for cancer therapy. Clin Cancer Res: J Am Assoc Cancer Res. 2009;15:2583–7.
15. Conkright M, Montminy M. CREB: the unindicted cancer co-conspirator. Trends Cell Biol. 2005;15:457–9.
16. Steven A, Heiduk M, Recktenwald CV, Hiebl B, Wickenhauser C, Massa C, et al. Colorectal Carcinogenesis: Connecting K-RAS-Induced Transformation and CREB Activity In Vitro and In Vivo. Mol Cancer Res. 2015;13:1248–62.
17. Li B, Zheng L, Ye J, Zhang C, Zhou J, Huang Q, et al. CREB1 contributes colorectal cancer cell plasticity by regulating lncRNA CCAT1 and NF-kappaB pathways. Sci China Life Sci. 2022;65:1481–97.
18. Luna MA. Salivary mucoepidermoid carcinoma: revisited. Adv Anat Pathol. 2006;13:293–307.
19. O'Neill ID. t(11;19) translocation and CRTC1-MAML2 fusion oncogene in mucoepidermoid carcinoma. Oral Oncol. 2009;45:2–9.
20. Chen Z, Ni W, Li JL, Lin S, Zhou X, Sun Y. he CRTC1-MAML2 fusion is the major oncogenic driver in mucoepidermoid carcinoma. JCI Insight. 2021;6:e139497.
21. Chen J, Li JL, Chen Z, Griffin JD, Wu L. Gene expression profiling analysis of CRTC1-MAML2 fusion oncogene-induced transcriptional program in human mucoepidermoid carcinoma cells. BMC Cancer. 2015;15:803.
22. Wu L, Liu J, Gao P, Nakamura M, Cao Y, Shen H, et al. Transforming activity of MECT1-MAML2 fusion oncoprotein is mediated by constitutive CREB activation. EMBO J. 2005;24:2391–402.
23. Komiya T, Park Y, Modi S, Coxon AB, Oh H, Kaye FJ. Sustained expression of Mect1-Maml2 is essential for tumor cell growth in salivary gland cancers carrying the t(11;19) translocation. Oncogene. 2006;25:6128–32.
24. Amelio AL, Fallahi M, Schaub FX, Zhang M, Lawani MB, Alperstein AS, et al. CRTC1/MAML2 gain-of-function interactions with MYC create a gene signature predictive of cancers with CREB-MYC involvement. Proc Natl Acad Sci USA. 2014;111:E3260–E8.
25. Musicant AM, Parag-Sharma K, Gong W, Sengupta M, Chatterjee A, Henry EC, et al. CRTC1/MAML2 directs a PGC-1alpha-IGF-1 circuit that confers vulnerability to PPARgamma inhibition. Cell Rep. 2021;34:108768.
26. Batsakis JG. Salivary gland neoplasia: an outcome of modified morphogenesis and cytodifferentiation. Oral Surg Oral Med Oral Pathol. 1980;49:229–32.
27. Brandwein MS, Ivanov K, Wallace DI, Hille JJ, Wang B, Fahmy A, et al. Mucoepidermoid carcinoma: a clinicopathologic study of 80 patients with special reference to histological grading. Am J Surg Pathol. 2001;25:835–45.
28. Goode RK, Auclair PL, Ellis GL. Mucoepidermoid carcinoma of the major salivary glands: clinical and histopathologic analysis of 234 cases with evaluation of grading criteria. Cancer. 1998;82:1217–24.
29. Katabi N, Ghossein R, Ali S, Dogan S, Klimstra D, Ganly I. Prognostic features in mucoepidermoid carcinoma of major salivary glands with emphasis on tumour histologic grading. Histopathology. 2014;65:793–804.
30. Hicks MJ, el-Naggar AK, Byers RM, Flaitz CM, Luna MA, Batsakis JG. Prognostic factors in mucoepidermoid carcinomas of major salivary glands: a clinicopathologic and flow cytometric study. Eur J Cancer B Oral Oncol. 1994;30B:329–34.
31. Spiro RH, Huvos AG, Berk R, Strong EW. Mucoepidermoid carcinoma of salivary-gland origin - clinicopathologic study of 367 cases. Am J Surg. 1978;136:461–8.
32. Fonseca I, Clode AL, Soares J. Mucoepidermoid carcinoma of major and minor salivary glands: a survey of 43 cases with study of prognostic indicators. Int J Surg Pathol. 1993;1:3–12.
33. Saitou M, Gaylord EA, Xu E, May AJ, Neznanova L, Nathan S, et al. Functional specialization of human salivary glands and origins of proteins intrinsic to human saliva. Cell Rep. 2020;33:108402.
34. Chen S, Zhou Y, Chen Y, Gu J. fastp: an ultra-fast all-in-one FASTQ preprocessor. Bioinformatics. 2018;34:i884–i90.
35. Dobin A, Davis CA, Schlesinger F, Drenkow J, Zaleski C, Jha S, et al. STAR: ultrafast universal RNA-seq aligner. Bioinformatics. 2013;29:15–21.
36. Patro R, Duggal G, Love MI, Irizarry RA, Kingsford C. Salmon provides fast and bias-aware quantification of transcript expression. Nat Methods. 2017;14:417–9.
37. Love MI, Huber W, Anders S. Moderated estimation of fold change and dispersion for RNA-seq data with DESeq2. Genome Biol. 2014;15:550.
38. Huber W, Carey VJ, Gentleman R, Anders S, Carlson M, Carvalho BS, et al. Orchestrating high-throughput genomic analysis with Bioconductor. Nat Methods. 2015;12:115–21.
39. Subramanian A, Tamayo P, Mootha VK, Mukherjee S, Ebert BL, Gillette MA, et al. Gene set enrichment analysis: a knowledge-based approach for interpreting genome-wide expression profiles. Proc Natl Acad Sci USA. 2005;102:15545–50.
40. Liberzon A, Birger C, Thorvaldsdottir H, Ghandi M, Mesirov JP, Tamayo P. The Molecular Signatures Database (MSigDB) hallmark gene set collection. Cell Syst. 2015;1:417–25.
41. Grossman RL, Heath AP, Ferretti V, Varmus HE, Lowy DR, Kibbe WA, et al. Toward a shared vision for cancer genomic data. N Engl J Med. 2016;375:1109–12.
42. Shen S, Park JW, Lu ZX, Lin L, Henry MD, Wu YN, et al. rMATS: robust and flexible detection of differential alternative splicing from replicate RNA-Seq data. Proc Natl Acad Sci. 2014;111:E5593–E601.
43. Ramirez F, Ryan DP, Gruning B, Bhardwaj V, Kilpert F, Richter AS, et al. deepTools2: a next generation web server for deep-sequencing data analysis. Nucleic Acids Res. 2016;44:W160–W5.
44. Roulis M, Nikolaou C, Kotsaki E, Kaffe E, Karagianni N, Koliaraki V, et al. Intestinal myofibroblast-specific Tpl2-Cox-2-PGE2 pathway links innate sensing to epithelial homeostasis. Proc Natl Acad Sci USA. 2014;111:E4658–E67.

45. Blum R, Gupta R, Burger PE, Ontiveros CS, Salm SN, Xiong X, et al. Molecular signatures of prostate stem cells reveal novel signaling pathways and provide insights into prostate cancer. PLoS One. 2009;4:e5722.
46. Damrauer JS, Roell KR, Smith MA, Sun X, Kirk EL, Hoadley KA, et al. Identification of a Novel Inflamed Tumor Microenvironment Signature as a Predictive Biomarker of Bacillus Calmette-Guerin Immunotherapy in Non-Muscle-Invasive Bladder Cancer. Clin Cancer Res. 2021;27:4599–609.
47. Maruyama EO, Aure MH, Xie X, Myal Y, Gan L, Ovitt CE. Cell-specific Cre strains for genetic manipulation in salivary glands. PLoS One. 2016;11:e0146711.
48. Shi G, Zhu L, Sun Y, Bettencourt R, Damsz B, Hruban RH, et al. Loss of the acinar-restricted transcription factor Mist1 accelerates Kras-induced pancreatic intraepithelial neoplasia. Gastroenterology. 2009;136:1368–78.
49. Schaub FX, Reza MS, Flaveny CA, Li W, Musicant AM, Hoxha S, et al. Fluorophore-NanoLuc BRET reporters enable sensitive in vivo optical imaging and flow cytometry for monitoring tumorigenesis. Cancer Res. 2015;75:5023–33.
50. Carper MB, Troutman S, Wagner BL, Byrd KM, Selitsky SR, Parag-Sharma K, et al. An immunocompetent mouse model of HPV16(+) head and neck squamous cell carcinoma. Cell Rep. 2019;29:1660–74.
51. Detre S, Saclani Jotti G, Dowsett M. A "quickscore" method for immunohistochemical semiquantitation: validation for oestrogen receptor in breast carcinomas. J Clin Pathol. 1995;48:876–8.
52. Tonon G, Modi S, Wu L, Kubo A, Coxon A, Komiya T, et al. t(11;19)(q21;p13) translocation in mucoepidermoid carcinoma creates a novel fusion product that disrupts a Notch signaling pathway. Nat Genet. 2003;33:208–13.
53. Young L, Sung J, Stacey G, Masters JR. Detection of mycoplasma in cell cultures. Nat Protoc. 2010;5:929–34.
54. Spike BT, Engle DD, Lin JC, Cheung SK, La J, Wahl GM. A mammary stem cell population identified and characterized in late embryogenesis reveals similarities to human breast cancer. Cell Stem Cell. 2012;10:183–97.
55. Stanger BZ, Wahl GM. Cancer as a disease of development gone awry. Annu Rev Pathol. 2024;19:397–421.
56. Sole L, Lobo-Jarne T, Alvarez-Villanueva D, Alonso-Maranon J, Guillen Y, Guix M, et al. p53 wild-type colorectal cancer cells that express a fetal gene signature are associated with metastasis and poor prognosis. Nat Commun. 2022;13:2866.
57. Janky R, Verfaillie A, Imrichova H, Van de Sande B, Standaert L, Christiaens V, et al. iRegulon: from a gene list to a gene regulatory network using large motif and track collections. PLoS Comput Biol. 2014;10:e1003731.
58. Pandit B, Halasi M, Gartel AL. p53 negatively regulates expression of FoxM1. Cell Cycle. 2009;8:3425–7.
59. Barsotti AM, Prives C. Pro-proliferative FoxM1 is a target of p53-mediated repression. Oncogene. 2009;28:4295–305.
60. Hingorani SR, Wang L, Multani AS, Combs C, Deramaudt TB, Hruban RH, et al. Trp53R172H and KrasG12D cooperate to promote chromosomal instability and widely metastatic pancreatic ductal adenocarcinoma in mice. Cancer Cell. 2005;7:469–83.
61. Wang K, McDermott JD, Schrock AB, Elvin JA, Gay L, Karam SD, et al. Comprehensive genomic profiling of salivary mucoepidermoid carcinomas reveals frequent BAP1, PIK3CA, and other actionable genomic alterations. Ann Oncol. 2017;28:748–53.
62. Wang X, Bai J, Yan J, Li B. The clinical outcome, pathologic spectrum, and genomic landscape for 454 cases of salivary mucoepidermoid carcinoma. NPJ Precis Oncol. 2024;8:238.
63. Gomes CC, Diniz MG, Orsine LA, Duarte AP, Fonseca-Silva T, Conn BI, et al. Assessment of TP53 mutations in benign and malignant salivary gland neoplasms. PLoS One. 2012;7:e41261.
64. Rodriguez-Ramirez C, Zhang Z, Warner KA, Herzog AE, Mantesso A, Zhang Z, et al. p53 inhibits Bmi-1-driven self-renewal and defines salivary gland cancer stemness. Clin Cancer Res. 2022;28:4757–70.
65. Andrews A, Warner K, Rodriguez-Ramirez C, Pearson AT, Nor F, Zhang Z, et al. Ablation of cancer stem cells by therapeutic inhibition of the MDM2-p53 interaction in mucoepidermoid carcinoma. Clin Cancer Res. 2019;25:1588–600.
66. Jaskoll T, Htet K, Abichaker G, Kaye FJ, Melnick M. CRTC1 expression during normal and abnormal salivary gland development supports a precursor cell origin for mucoepidermoid cancer. Gene Expr Patterns. 2011;11:57–63.
67. Adams A, Warner K, Pearson AT, Zhang Z, Kim HS, Mochizuki D, et al. ALDH/CD44 identifies uniquely tumorigenic cancer stem cells in salivary gland mucoepidermoid carcinomas. Oncotarget. 2015;6:26633–50.
68. Ninche N, Kwak M, Ghazizadeh S Diverse epithelial cell populations contribute to the regeneration of secretory units in injured salivary glands. Development. 2020;147.
69. Batsakis JG, Regezi JA, Luna MA, el-Naggar A. Histogenesis of salivary gland neoplasms: a postulate with prognostic implications. J Laryngol Otol. 1989;103:939–44.
70. May AJ, Cruz-Pacheco N, Emmerson E, Gaylord EA, Seidel K, Nathan S, et al. Diverse progenitor cells preserve salivary gland ductal architecture after radiation-induced damage. Development. 2018;145.
71. Aure MH, Konieczny SF, Ovitt CE. Salivary gland homeostasis is maintained through acinar cell self-duplication. Dev Cell. 2015;33:231–7.
72. Vasioukhin V, Degenstein L, Wise B, Fuchs E. The magical touch: genome targeting in epidermal stem cells induced by tamoxifen application to mouse skin. Proc Natl Acad Sci USA. 1999;96:8551–6.
73. Nitta M, Kume T, Nogawa H. FGF alters epithelial competence for EGF at the initiation of branching morphogenesis of mouse submandibular gland. Dev Dynam. 2009;238:315–23.
74. Aure MH, Symonds JM, Villapudua CU, Dodge JT, Werner S, Knosp WM, et al. FGFR2 is essential for salivary gland duct homeostasis and MAPK-dependent seromucous acinar cell differentiation. Nat Commun. 2023;14:6485.
75. Mattingly A, Finley JK, Knox SM. Salivary gland development and disease. Wiley Interdiscip Rev Dev Biol. 2015;4:573–90.
76. Xie Y, Su N, Yang J, Tan Q, Huang S, Jin M, et al. FGF/FGFR signaling in health and disease. Signal Transduct Target Ther. 2020;5:181.
77. Beenken A, Mohammadi M. The FGF family: biology, pathophysiology and therapy. Nat Rev Drug Discov. 2009;8:235–53.
78. Wang S, Sekiguchi R, Daley WP, Yamada KM. Patterned cell and matrix dynamics in branching morphogenesis. J Cell Biol. 2017;216:559–70.
79. Hsu JC, Yamada KM. Salivary gland branching morphogenesis-recent progress and future opportunities. Int J Oral Sci. 2010;2:117–26.
80. Musselmann K, Green JA, Sone K, Hsu JC, Bothwell IR, Johnson SA, et al. Salivary gland gene expression atlas identifies a new regulator of branching morphogenesis. J Dent Res. 2011;90:1078–84.
81. Yeh BK, Igarashi M, Eliseenkova AV, Plotnikov AN, Sher I, Ron D, et al. Structural basis by which alternative splicing confers specificity in fibroblast growth factor receptors. Proc Natl Acad Sci USA. 2003;100:2266–71.
82. Finburgh EN, Mauduit O, Noguchi T, Bu JJ, Abbas AA, Hakim DF, et al. Role of FGF10/FGFR2b Signaling in Homeostasis and Regeneration of Adult Lacrimal Gland and Corneal Epithelium Proliferation. Invest Ophthalmol Vis Sci. 2023;64:21.
83. Epstein RJ, Tian LJ, Gu YF. 2b or not 2b: how opposing FGF receptor splice variants are blocking progress in precision oncology. J Oncol. 2021;2021:9955456.
84. Holzmann K, Grunt T, Heinzle C, Sampl S, Steinhoff H, Reichmann N, et al. Alternative Splicing of Fibroblast Growth Factor Receptor IgIII Loops in Cancer. J Nucleic Acids. 2012;2012:950508.
85. Amelio AL, Caputi M, Conkright MD. Bipartite functions of the CREB co-activators selectively direct alternative splicing or transcriptional activation. EMBO J. 2009;28:2733–47.
86. Tasoulas J, Srivastava S, Xu X, Tarasova V, Maniakas A, Karreth FA, et al. Genetically engineered mouse models of head and neck cancers. Oncogene. 2023;42:2593–609.
87. Lombaert IM, Abrams SR, Li L, Eswarakumar VP, Sethi AJ, Witt RL, et al. Combined KIT and FGFR2b signaling regulates epithelial progenitor expansion during organogenesis. Stem Cell Rep. 2013;1:604–19.
88. Emmerson E, Knox SM. Salivary gland stem cells: a review of development, regeneration and cancer. Genesis. 2018;56:e23211.
89. Chatzeli L, Bordeu I, Han S, Bisetto S, Waheed Z, Koo BK, et al. A cellular hierarchy of Notch and Kras signaling controls cell fate specification in the developing mouse salivary gland. Dev Cell. 2023;58:94–109.
90. Mantovani F, Collavin L, Del Sal G. Mutant p53 as a guardian of the cancer cell. Cell Death Differ. 2019;26:199–212.
91. Bieging KT, Mello SS, Attardi LD. Unravelling mechanisms of p53-mediated tumour suppression. Nat Rev Cancer. 2014;14:359–70.
92. Rodriguez-Ramirez C, Nor JE. p53 and cell fate: sensitizing head and neck cancer stem cells to chemotherapy. Crit Rev Oncog. 2018;23:173–87.
93. Kiyoshima T, Shima K, Kobayashi I, Matsuo K, Okamura K, Komatsu S, et al. Expression of p53 tumor suppressor gene in adenoid cystic and mucoepidermoid carcinomas of the salivary glands. Oral Oncol. 2001;37:315–22.
94. Katoh M, Loriot Y, Brandi G, Tavolari S, Wainberg ZA, Katoh M. FGFR-targeted therapeutics: clinical activity, mechanisms of resistance and new directions. Nat Rev Clin Oncol. 2024;21:312–29.
95. Shoji K, Teishima J, Hayashi T, Ohara S, McKeehan WL, Matsubara A. Restoration of fibroblast growth factor receptor 2IIIb enhances the chemosensitivity of human prostate cancer cells. Oncol Rep. 2014;32:65–70.
96. Matsubara A, Teishima J, Mirkhat S, Yasumoto H, Mochizuki H, Seki M, et al. Restoration of FGF receptor type 2 enhances radiosensitivity of hormone-refractory human prostate carcinoma PC-3 cells. Anticancer Res. 2008;28:2141–6.
97. Varghese JJ, Schmale IL, Wang Y, Hansen ME, Newlands SD, Ovitt CE, et al. Retroductal nanoparticle injection to the murine submandibular gland. J Vis Exp. 2018;e7521. https://doi.org/10.3791/57521.
98. Troester MA, Herschkowitz JI, Oh DS, He X, Hoadley KA, Barbier CS, et al. Gene expression patterns associated with p53 status in breast cancer. BMC Cancer. 2006;6:276.

ACKNOWLEDGEMENTS

We are grateful for the support of previous and current members of the Amelio lab, with special thanks to Dr. Harish Bharambe for his technical expertise and assistance.

We would also like to thank Gabriela De La Cruz and Bentley Midkiff in the Pathology Services Core and David Corcoran in the Lineberger Bioinformatics Core of the University of North Carolina at Chapel Hill for expert technical assistance with histological staining and fluorescent imaging. The Pathology Services Core is supported in part by an NCI Center Core Support Grant (P30-CA016086). In addition, the authors would like to acknowledge Dr. Jimena Guidice and Dr. Jessica Cote for their technical assistance. This work was also supported in part by Dr. Joseph Johnson and Brooke Smedley of the Analytic Microscopy Core, Jodi Balasi of the Tissue Core, and Dr. Mikalai Budzevich and Epi Ruiz of the Small Animal Imaging Lab at the Moffitt Cancer Center and Research Institute, a comprehensive cancer center designated by the National Cancer Institute and funded in part by Moffitt's Cancer Center Support Grant (P30-CA076292). This work was supported in part by NIH/NIGMS T32-GM007092 and NIH/NIDCR F31-DE027282 training grants (to AMM), Head and Neck Cancer Fund (to TGH and DNH), NIH/NCATS-supported UL1-TR002489 UNC Translational Team Science Award (TTSA#026P1; to TGH and ALA), Moffitt Cancer Center funds (to ALA), and NIH/NIDCR R01-DE030123 (to ALA).

AUTHOR CONTRIBUTIONS

Conception and design: AMM, JMRB, and ALA. Development of methodology: AMM, JMRB, JSD, JHM, LJBL, Y-HT, and ALA. Acquisition of data (provided reagents, provided facilities, etc.): AMM, JMRB, JP, RB, and RS. Interpretation of data (e.g., statistical analysis, biostatistics, computational analysis): AMM, JMRB, JSD, JHM, LJBL, Y-HT, JM, OG, SMK, and ALA. Writing of the manuscript: AMM, JMRB, and ALA. Review and revision of the manuscript: AMM, JMRB, JSD, JHM, LJBL, Y-HT, JM, JP, RB, RS, RJP, JCH-P, DNH, TGH, OG, SMK, and ALA. Administrative, technical, or material support (i.e., reporting or organizing data, constructing databases): JM, LJBL, Y-HT, JHM, RB, RS, OG, SMK, and ALA. Study supervision: OG, SMK, and ALA. Acquisition of funding: TGH and ALA.

COMPETING INTERESTS

The authors declare no competing interests.

ETHICS APPROVAL

Research involving human tissues was reviewed and approved by the Institutional Review Boards at The University of North Carolina at Chapel Hill (IRB protocols 15-1604 and 17-2947) and University of California—San Francisco (IRB protocol 10-00768) and informed consent was obtained from all participants. Research involving murine tissues was reviewed and approved by the Institutional Animal Care and Use Committee (IACUC) of The University of North Carolina Chapel Hill (IACUC protocols 17-202 and 20-142), Moffitt Cancer Center and the University of South Florida (IACUC protocols 11291 M and 11379 R). All methods were performed in accordance with relevant guidelines and regulations.

ADDITIONAL INFORMATION

Supplementary information The online version contains supplementary material available at https://doi.org/10.1038/s41388-025-03444-7.

Correspondence and requests for materials should be addressed to Antonio L. Amelio.

Reprints and permission information is available at http://www.nature.com/reprints

Publisher's note Springer Nature remains neutral with regard to jurisdictional claims in published maps and institutional affiliations.

[1]Graduate Curriculum in Genetics and Molecular Biology, Biological and Biomedical Sciences Program, School of Medicine, The University of North Carolina at Chapel Hill, Chapel Hill, NC, USA. [2]Cancer Biology PhD Program, University of South Florida, Tampa, FL, USA. [3]Department of Tumor Microenvironment and Metastasis, H. Lee Moffitt Cancer Center & Research Institute, Tampa, FL, USA. [4]Department of Medicine, Division of Oncology, School of Medicine, The University of North Carolina at Chapel Hill, Chapel Hill, NC, USA. [5]Bioinformatics Core, Lineberger Comprehensive Cancer Center, School of Medicine, The University of North Carolina at Chapel Hill, Chapel Hill, NC, USA. [6]Department of Biological Sciences, University at Buffalo, Buffalo, NY, USA. [7]Department of Pathology and Laboratory Medicine, School of Medicine, The University of North Carolina at Chapel Hill, Chapel Hill, NC, USA. [8]Center for Cancer Research, University of Tennessee Health Sciences Center, Memphis, TN, USA. [9]Division of Diagnostic Sciences, Adams School of Dentistry, University of North Carolina at Chapel Hill, Chapel Hill, NC, USA. [10]Department of Pathology, H. Lee Moffitt Cancer Center & Research Institute, Tampa, FL, USA. [11]Department of Otolaryngology/Head and Neck Surgery, School of Medicine, The University of North Carolina at Chapel Hill, Chapel Hill, NC, USA. [12]Department of Cell and Tissue Biology, University of California San Francisco, San Francisco, CA, USA. [13]Program in Craniofacial Biology, University of California San Francisco, San Francisco, CA, USA. [14]Department of Head and Neck-Endocrine Oncology, H. Lee Moffitt Cancer Center & Research Institute, Tampa, FL, USA. [15]These authors contributed equally: Adele M. Musicant, Julia M. R. Billington. ✉email: antonio.amelio@moffitt.org